



SCUOLA INTERNAZIONALE SUPERIORE DI STUDI AVANZATI

SISSA Digital Library

Evolution of Galaxy Star Formation and Metallicity: Impact on Double Compact Object Mergers

Original

Evolution of Galaxy Star Formation and Metallicity: Impact on Double Compact Object Mergers / Boco, L.; Lapi, A.; Chruslinska, M.; Donevski, D.; Sicilia, A.; Danese, L.. - In: THE ASTROPHYSICAL JOURNAL. - ISSN 1538-4357. - 907:2(2021), pp. 1-15. [10.3847/1538-4357/abd3a0]

Availability:

This version is available at: 20.500.11767/118409 since: 2021-02-16T09:03:38Z

Publisher:

Published

DOI:10.3847/1538-4357/abd3a0

Terms of use:

Testo definito dall'ateneo relativo alle clausole di concessione d'uso




Publisher copyright

note finali coverpage

(Article begins on next page)



Evolution of Galaxy Star Formation and Metallicity: Impact on Double Compact Object Mergers

L. Boco^{1,2,3} , A. Lapi^{1,2,3,4} , M. Chruslinska⁵, D. Donevski¹ , A. Sicilia¹, and L. Danese^{1,2}

¹ SISSA, Via Bonomea 265, I-34136 Trieste, Italy

² IFPU-Institute for Fundamental Physics of the Universe, Via Beirut 2, I-34014 Trieste, Italy

³ INFN-Sezione di Trieste, via Valerio 2, I-34127 Trieste, Italy

⁴ INAF-Osservatorio Astronomico di Trieste, via Tiepolo 11, I-34131 Trieste, Italy

⁵ Department of Astrophysics/IMAPP, Radboud University, P.O. Box 9010, NL-6500 GL Nijmegen, The Netherlands

Received 2020 November 4; revised 2020 December 4; accepted 2020 December 10; published 2021 February 5

Abstract

In this paper, we study the impact of different galaxy statistics and empirical metallicity scaling relations on the merging rates and properties of compact object binaries. Firstly, we analyze the similarities and differences of using the star formation rate functions versus stellar mass functions as galaxy statistics for the computation of cosmic star formation rate density. We then investigate the effects of adopting the Fundamental Metallicity Relation versus a classic Mass Metallicity Relation to assign metallicity to galaxies with given properties. We find that when the Fundamental Metallicity Relation is exploited, the bulk of the star formation occurs at relatively high metallicities, even at high redshift; the opposite holds when the Mass Metallicity Relation is employed, since in this case the metallicity at which most of the star formation takes place strongly decreases with redshift. We discuss the various reasons and possible biases giving rise to this discrepancy. Finally, we show the impact of these different astrophysical prescriptions on the merging rates and properties of compact object binaries; specifically, we present results for the redshift-dependent merging rates and for the chirp mass and time delay distributions of the merging binaries.

Unified Astronomy Thesaurus concepts: Galaxy evolution (594); Early-type galaxies (429); Luminosity function (942); Stellar mass functions (1612); Metallicity (1031); Stellar mergers (2157); Compact objects (288); Star formation (1569); Gravitational wave sources (677); Gravitational waves (678); Astrophysical black holes (98); Neutron stars (1108)

1. Introduction

The discovery of gravitational waves (GWs) by the LIGO/Virgo team (Abbott et al. 2016a, 2016b, 2016c, 2017a, 2017b, 2017c, 2017d, 2017e, 2019, 2020a, 2020b; also <https://www.ligo.org/>) has opened a new observational window to study the universe. On the one hand, even a few GW events with detected electromagnetic counterparts are of enormous importance for cosmology and fundamental physics (Creminelli & Vernizzi 2017; Radice et al. 2018; Yang et al. 2019); on the other hand, the large statistics of GWs may yield substantial astrophysical information in relation to stellar and binary evolution (e.g., Belczynski et al. 2016; Dvorkin et al. 2018; Giacobbo & Mapelli 2018), the properties of the host galaxies such as chemical evolution, star formation histories (SFHs), initial mass function (IMF; e.g., O’Shaughnessy et al. 2010; de Mink & Belczynski 2015), and even cosmology in general (e.g., Taylor & Gair 2012; Nissanke et al. 2013; Liao et al. 2017; Fishbach et al. 2019). Moreover, the potential to cross-correlate GW detected signals with some other tracers of Large-Scale Structures can help to improve cosmological constraints or to test competing astrophysical frameworks (e.g., Oguri 2016; Raccanelli et al. 2016; Scelfo et al. 2018, 2020; Calore et al. 2020).

Given these numerous applications, it is important to properly characterize the population of compact object (CO) merging binaries, to compute the related merging rates and to understand their dependence on different astrophysical scenarios. The merging rates per unit volume and chirp mass \mathcal{M}^6 as a function of cosmic time can be computed as (see Barrett et al. 2018 and

Neijssel et al. 2019):

$$\frac{d\dot{N}}{dVd\mathcal{M}}(t) = \int dt_d \int dZ \frac{dN}{dM_{\text{SFR}} d\mathcal{M} dt_d}(Z) \frac{d\dot{M}_{\text{SFR}}}{dVdZ}(t - t_d) \quad (1)$$

where t is the cosmic time, equivalent to redshift, M_{SFR} is the star formed mass, t_d is the delay time between the formation of the progenitor binary and the merging of the COs binary, Z is the metallicity, and V the comoving cosmological volume.

The first term in the integral $dN/dM_{\text{SFR}} d\mathcal{M} dt_d$ is related to stellar and binary evolution, and represents the number of merging double compact objects (DCOs) per unit of star-forming mass per bin of chirp mass and time delay. This can be evaluated via stellar and binary evolution simulations (see, e.g., Dominik et al. 2012, 2015; de Mink et al. 2013; de Mink & Belczynski 2015; Belczynski et al. 2016; Spera & Mapelli 2017; Chruslinska et al. 2018; Giacobbo & Mapelli 2018; Mapelli & Giacobbo 2018; Spera et al. 2019; Santoliquido et al. 2020). Various processes involved in stellar and binary evolution depend on metallicity (e.g., radiation-driven stellar wind mass loss rates, core-collapse physics, mass transfer characteristics and stability), so the number of merging BH/NS binaries constituting the per unit mass formed in stars also varies with this quantity.

The second term, $d\dot{M}_{\text{SFR}}/dV dZ$, is related to galaxy evolution: it represents the star-forming mass per units of time, comoving volume, and metallicity, i.e., it is the star formation rate (SFR) density per metallicity bin. There are two main ways to estimate this: exploiting the results of cosmological simulations (e.g., Mapelli et al. 2017; O’Shaughnessy et al. 2017;

⁶ The chirp mass is defined as: $\mathcal{M} \equiv (m_1 m_2)^{3/5} / (m_1 + m_2)^{1/5}$, where m_1 and m_2 are the masses of the two merging objects.

Lamberts et al. 2018; Mapelli & Giacobbo 2018; Artale et al. 2019), or the use of empirical recipes concerning the cosmic SFR density and metallicity distributions inferred from observations (e.g., Belczynski et al. 2016; Lamberts et al. 2016; Cao et al. 2018; Elbert et al. 2018; Li et al. 2018; Boco et al. 2019; Chruslinska & Nelemans 2019; Neijssel et al. 2019; Santoliquido et al. 2020).

The main focus of this work is to revise the different empirical approaches pursued to compute the galactic term, and to attempt to quantify the impact of different choices and understand their advantages and drawbacks; moreover, we propose new ways to compute this. We stress that the methods discussed in this paper to compute the galactic term are purely based on observations and on empirically derived scaling relations, and do not rely on semi-analytical models or simulations. Finally, we study the effects of the different prescriptions on the merging rates and properties of merging binaries.

The plan of the paper is as follows: In Section 2 we compare the two main empirical methods of computing cosmic SFR density: via luminosity/SFR functions (SFRF) or via galactic stellar mass functions (GSMF) and the main sequence (MS) of star-forming galaxies. In Section 3 we present the two main scaling relations to empirically assign metallicity to galaxies (the Fundamental Metallicity Relation (FMR) or a Mass Metallicity Relation (MZR)) and we compute the galactic term $dM_{\text{SFR}}/dV dZ$, combining the two possible metallicity scaling relations with the two types of galaxy statistics. In Section 4, we compute the merging rates and some properties of compact binaries for these different prescriptions, based on the outcomes of the STARTRACK binary evolution simulations, so as to compute the stellar factor $dN/dM_{\text{SFR}} dM_* dt_d$. Finally, in Section 5 we summarize our main findings.

Throughout this work, we rely on the standard flat Λ CDM cosmology (Planck Collaboration 2019) with cosmological parameters: $\Omega_M = 0.32$, $\Omega_b = 0.05$, $H_0 = 67 \text{ km s}^{-1} \text{ Mpc}^{-1}$. The Chabrier IMF (2003, 2005; see also Mo et al. 2010) is adopted, with mass range $0.08\text{--}150 M_\odot$. A value $Z_\odot = 0.0153$ for solar metallicity, and $12 + \log(\text{O}/\text{H})_\odot = 8.76$ is adopted for solar oxygen abundance (Caffau et al. 2011).

2. Cosmic SFR and Galaxy Statistics

The first important ingredient in the computation of the factor $dM_{\text{SFR}}/dV dZ$ is constituted by the cosmic SFR density dM_{SFR}/dV , representing the average rate at which new stars are formed in the universe at different redshifts per unit comoving volume. There are two different ways to compute and exploit this, as discussed below.

2.1. SFR/Luminosity Functions

The most direct approach to computing cosmic SFR density relies on the galaxies' star formation rate functions (SFRF), $dN/dV d \log \psi$, at different redshifts, representing the number density of galaxies per logarithmic bin of SFR (ψ). The SFRF can be computed from the UV and IR luminosity functions of galaxies (see Mancuso et al. 2016a; Boco et al. 2019), since luminosity can be converted into SFR (e.g., Kennicutt 1998; Kennicutt & Evans 2012).

In fact, the SFR of a galaxy can be related to its UV luminosity, which mainly comes from young, blue stars. However, since dust absorbs UV radiation and re-emits it in the mid- and far-IR band,

SFR estimated based solely on UV luminosities can be substantially underestimated. Nevertheless it is still possible, for galaxies with a relatively low SFR ($\psi \lesssim 30\text{--}50 M_\odot \text{ yr}^{-1}$) and relatively small dust content, to estimate SFR from UV data alone, using standard UV slope corrections (see Meurer et al. 1999; Calzetti et al. 2000; Bouwens et al. 2015). Therefore, the SFRF for $\psi \lesssim 30\text{--}50 M_\odot \text{ yr}^{-1}$ can be well constrained using data from deep UV surveys (see Wyder et al. 2005; Oesch et al. 2010; van der Burg et al. 2010; Cucciati et al. 2012; Finkelstein et al. 2015; Alavi et al. 2016; Bouwens et al. 2016, 2017; Bhatawdekar et al. 2019). Contrariwise, for highly star-forming galaxies with $\psi \gtrsim 30\text{--}50 M_\odot \text{ yr}^{-1}$, which are much richer in dust, UV corrections tend to fail (see Silva et al. 1998; Efstathiou et al. 2000; Coppin et al. 2015; Reddy et al. 2015; Fudamoto et al. 2017); as a consequence, estimates of SFR must be based on far-IR/(sub)mm wide-area surveys (see Lapi et al. 2011; Gruppioni et al. 2013, 2015; Magnelli et al. 2013; Gruppioni & Pozzi 2019). However, given the sensitivity limit of far-IR surveys, the shape of the SFR functions at the bright end becomes progressively uncertain at $z \gtrsim 3$. Nonetheless, relevant constraints in this regime have been obtained from deep radio surveys (Novak et al. 2017), from far-IR/(sub)millimeter stacking (see Rowan-Robinson et al. 2016; Dunlop et al. 2017) and super-deblending techniques (see Liu et al. 2018), and from targeted far-IR/(sub)millimeter observations of significant yet not complete samples of star-forming galaxies (e.g., Riechers et al. 2017; Marrone et al. 2018; Zavala et al. 2018) and quasar hosts (e.g., Venemans et al. 2017, 2018; Stacey et al. 2018). Moreover, very recently, Gruppioni et al. (2020) estimated the total IR luminosity functions up to redshift $z \lesssim 6$ based on a sample of 56 galaxies serendipitously detected by ALMA in the COSMOS and ECDFS fields, finding a pleasant agreement with previous far-IR/(sub)mm Herschel data, although still within large observational uncertainties.

The aforementioned set of data can be fitted via a simple Schechter function,

$$\frac{dN}{d \log \psi dV}(\psi, t) = \mathcal{N}(z) \left[\frac{\psi}{\psi_c(z)} \right]^{1-\alpha(z)} e^{-\psi/\psi_c(z)} \quad (2)$$

in terms of three fitting parameters: $\mathcal{N}(z)$, $\psi_c(z)$, and $\alpha(z)$ (see Table 1 of Mancuso et al. 2016a); in Figure 1, top panel, we show the data sets mentioned above, and the fitted SFRF. At $z \gtrsim 1$, heavily obscured, strongly star-forming galaxies populate the bright end of the SFR functions; these galaxies are the progenitors of local massive ellipticals (ETGs) with final stellar mass $M_* \gtrsim$ a few $\times 10^{10} M_\odot$. Mildly star-forming objects, in contrast, populate the faint end, and will end up as spheroid-like objects with rather low stellar mass ($\lesssim 10^{10} M_\odot$). Finally, late type disk galaxies (LTGs), with SFR of a few solar masses per year, are well traced by the UV-inferred SFR function at $z \lesssim 1$. This is also confirmed by the link between the SFRF and the stellar mass function of different morphological types, obtained via the continuity equation approach of Lapi et al. (2017).

From the SFRF, the cosmic SFR density can easily be estimated as:

$$\frac{dM}{dV}(t) = \int d \log \psi \psi \frac{dN}{d \log \psi dV}(\psi, t). \quad (3)$$

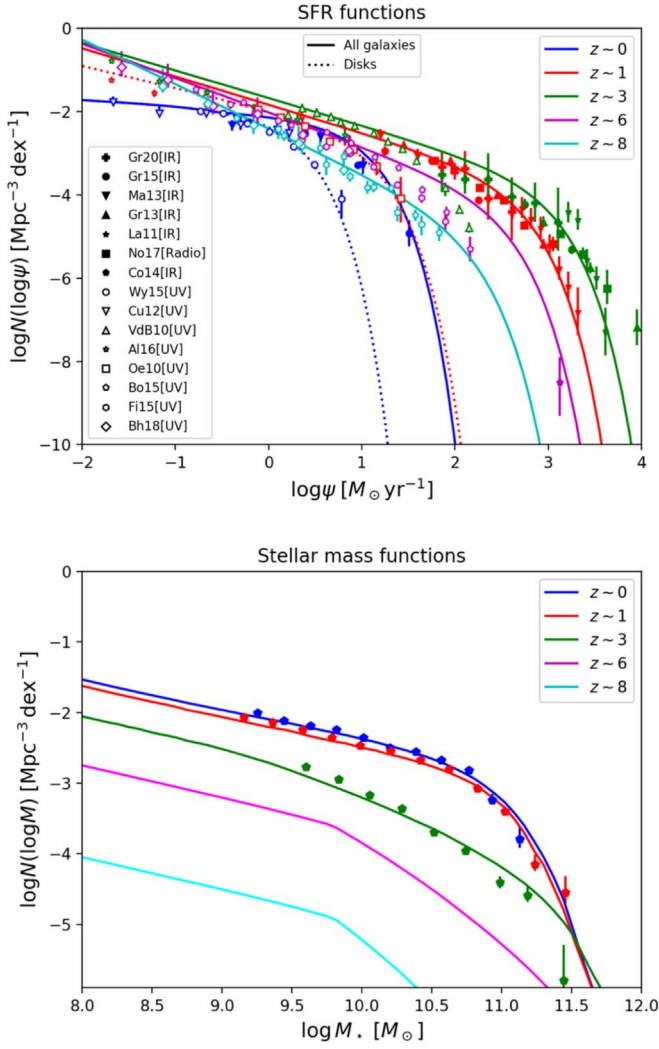


Figure 1. Top panel: SFR functions at redshifts $z = 0$ (blue), 1 (red), 3 (green), 6 (magenta), and 8 (cyan). Solid lines show the rendition from UV plus far-IR/(sub) millimeter/radio data, referring to the overall population of galaxies; dotted lines (only plotted at $z \simeq 0$ and 1) show the rendition from (dust-corrected) UV data, referring to disk galaxies. UV data (open symbols) are from van der Burg et al. (2010; triangles), Bouwens et al. (2016, 2017; pentagons), Finkelstein et al. (2015; hexagons), Cucciati et al. (2012; inverse triangles), Wyder et al. (2005; circles), Cucciati et al. (2010; squares), Alavi et al. (2016; stars), and Bhatawdekar et al. (2019; rhombus); far-IR/(sub)millimeter data (filled symbols) are from Gruppioni et al. (2020; filled plus), Gruppioni et al. (2015 circles), Magnelli et al. (2013; inverse triangles), Gruppioni et al. (2013; triangles), Lapi et al. (2011; stars), and Cooray et al. (2014; pentagons); radio data are from Novak et al. (2017 squares). Bottom panel: stellar mass functions for star-forming galaxies at redshifts $z = 0$ (blue), 1 (red), 3 (green), 6 (magenta), and 8 (cyan). Data points are taken from Davidzon et al. (2017).

The resulting determination of the cosmic SFR density is shown as a dotted–dashed black line in Figure 2. It can be observed that cosmic SFR computed in this way tends to be appreciably higher with respect to most of the previous determinations. This is due to the recent discovery, via the IR and far-IR/sub mm observations of Herschel and ALMA, of a significant number of dusty star-forming galaxies that are very attenuated or even invisible in the optical/UV bands. Such dusty galaxies, featuring an extremely high level of star formation ($\sim 50\text{--}3000 M_{\odot} \text{yr}^{-1}$), seem to have a significant impact on the total star formation at $2 \leq z \leq 6$ (see, e.g., Smail et al. 2012; Wang et al. 2019; Gruppioni et al. 2020). Therefore, since our SFRF fit is also based on data from recent

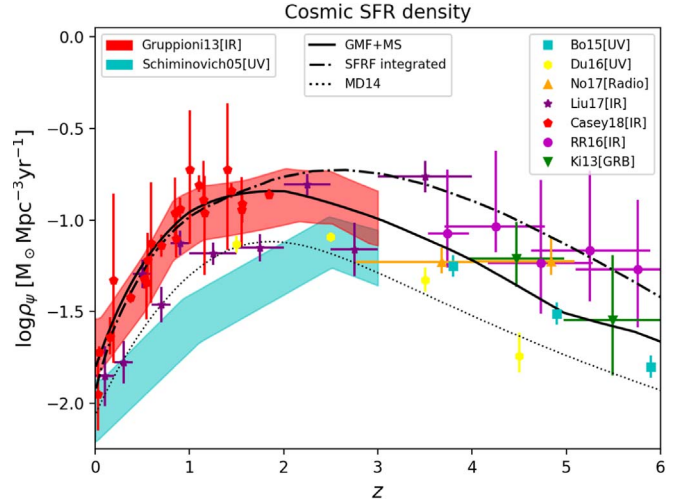


Figure 2. Cosmic SFR density as a function of redshift. The black solid line shows the result obtained by integrating the SFR functions reconstructed from the stellar mass functions plus the main sequence (Equation (5)). The black dotted–dashed line shows the result of the integration of the SFR functions (Equation (2)). For reference, the dotted line illustrates the determination by Madau & Dickinson (2014). Data are from (dust-corrected) UV observations by Schiminovich et al. (2005; cyan shaded area) and Bouwens et al. (2015; cyan squares); ALMA submillimeter observations of UV-selected galaxies on the HUDF are from Dunlop et al. (2017); VLA radio observations on the COSMOS field are from Novak et al. (2017), Herschel far-IR observations are from Gruppioni et al. (2013; red shaded area) and Casey et al. (2018; red pentagons); Herschel far-IR stacking is from Rowan-Robinson et al. (2016; magenta circles); far-IR/(sub)millimeter observations are taken from super-deblended data on the GOODS field in Liu et al. (2018), and estimates from long GRB rates are by Kistler et al. (2009, 2013; green reversed triangles).

far-IR/(sub)mm surveys, the resulting cosmic SFR density is larger and more in agreement with the recent IR data (see, e.g., Rowan-Robinson et al. 2016; Casey et al. 2018).

2.2. Stellar Mass Functions + Main Sequence

Another method for estimating cosmic SFR density is via convolving the stellar mass functions of star-forming galaxies at different redshifts with a distribution around the main sequence. This approach has been adopted in Chruslinska & Nelemans (2019); here, we review and improve it by adding a simple treatment of starburst galaxies.

A galaxy’s stellar mass is routinely estimated via near-IR data and broadband SED fitting (e.g., da Cunha et al. 2008; Boquien et al. 2019). Star-forming galaxies’ stellar mass function (GSMF) $dN/dV d \log M_{\star}$ has been determined at different redshifts by several authors (e.g., Ilbert et al. 2013; Muzzin et al. 2013; Tomczak et al. 2014; Davidzon et al. 2017). A good review of the different determinations can be found in Chruslinska & Nelemans (2019), where the authors provide an average fit between many different works. Here we adopt their fit, and in particular their prescription for a redshift-independent slope at the faint end (see Figure 1, bottom panel, and Figure 3 in Chruslinska & Nelemans 2019, solid lines).

In order to compute the cosmic SFR density, the GSMF must be convolved with a distribution of SFR around the main sequence (MS) of star-forming galaxies. The MS is a well known (approximately power-law) relation between the stellar mass of the galaxy and its SFR at a given redshift. This has been determined both observationally and theoretically in different works (see, e.g., Daddi et al. 2007; Rodighiero et al. 2011, 2015; Speagle et al. 2014; Whitaker et al. 2014; Schreiber et al. 2015;

Mancuso et al. 2016b; Dunlop et al. 2017; Bisigello et al. 2018; Pantoni et al. 2019; Lapi et al. 2020). However, we point out that MS shape and evolution with redshift is still debated, with relevant differences between various works; in particular, its behavior at large masses is very uncertain, with some authors advocating a possible flattening (although this may effectively be due to contamination from passive galaxies).

Note that the MS is only an average relation between mass and SFR; star-forming galaxies with fixed mass at a given redshift actually tend to be distributed in SFR following a double Gaussian shape (see Bethermin et al. 2012; Sargent et al. 2012; Ilbert et al. 2015; Schreiber et al. 2015). This bimodal distribution highlights the existence of two kind of galaxy populations: the dominant population of main sequence galaxies (MSGs), whose Gaussian distribution in SFR is centered around the MS value, and the subdominant population of starburst galaxies (SBG), whose Gaussian distribution is centered around a SFR typically $\sim 3\text{--}4\sigma$ above the MS value. In the aforementioned works it is empirically found that the shape of the distribution is almost independent of a galaxy's stellar mass and redshift. On the other hand, other recent studies, probing the SFR distribution of galaxies around the MS over a more extensive range of masses and redshifts, found an increase in starburst fractions at low masses $M_* \leq 10^9 M_\odot$ or at high redshifts $z \geq 2\text{--}3$ (see Caputi et al. 2017; Bisigello et al. 2018).

For the sake of simplicity, in this work we describe the galaxy distribution in SFR at fixed mass and redshift via a double Gaussian shape, with the same parameters as those indicated by Sargent et al. (2012), and with fixed starburst fractions in each redshift and mass bin:

$$\frac{dp}{d \log \psi}(\psi|z, M_*) = A_{\text{MS}} \exp\left[-\frac{(\log \psi - \langle \log \psi \rangle_{\text{MS}})^2}{2\sigma_{\text{MS}}^2}\right] + A_{\text{SB}} \exp\left[-\frac{(\log \psi - \langle \log \psi \rangle_{\text{SB}})^2}{2\sigma_{\text{SB}}^2}\right] \quad (4)$$

where $A_{\text{MS}} = 0.97$ is the fraction of MSG, $A_{\text{SB}} = 0.03$ the fraction of SBG; $\langle \log \psi \rangle_{\text{MS}}$ is the value given by the MS and which represents the central value for the first Gaussian, $\langle \log \psi \rangle_{\text{SB}} = \langle \log \psi \rangle_{\text{MS}} + 0.59$ is the central value of the second Gaussian, $\sigma_{\text{MS}} = 0.188$ is the one-sigma dispersion of the first Gaussian, and $\sigma_{\text{SB}} = 0.243$ is the dispersion of the starburst population.

Once the distribution in Equation (4) is convolved with the GSMF, one can reconstruct the SFRF of galaxies as follows:

$$\frac{dN_{\text{GSMF+MS}}}{d \log \psi dV}(z, \log \psi) = \int d \log M_* \frac{dN}{d \log M_* dV}(z, \log M_*) \times \frac{dp}{d \log \psi}(\log \psi|z, M_*) \quad (5)$$

In Sargent et al. (2012) and Ilbert et al. (2015) it is also demonstrated that such a convolution yields a good reconstruction of luminosity functions.

Integrating the reconstructed SFRF in the Equation above over the whole range of star formation, as in Equation (3), we obtain the cosmic SFR density as a function of cosmic time. In Figure 2 we show the cosmic SFR density computed by

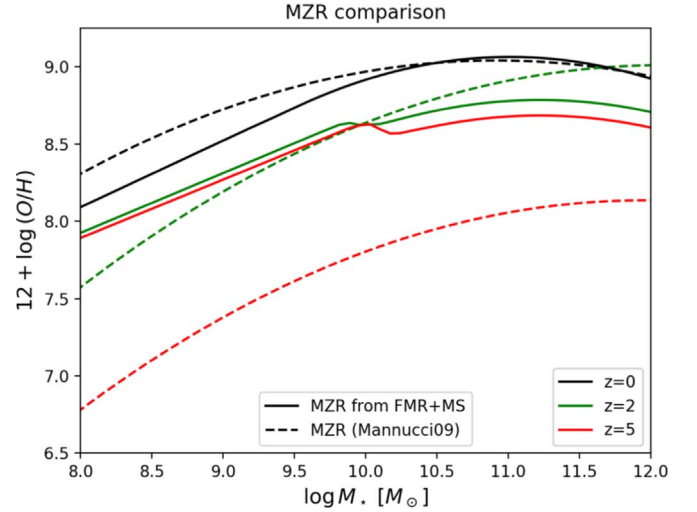


Figure 3. The average MZR relation ($\langle Z_{\text{MZR}} \rangle$), computed by convolving the FMR of Mannucci et al. (2011) with the MS at different redshifts (solid lines), compared with the MZR determination of Mannucci et al. (2009) at different redshifts (dashed lines).

integrating the SFRF directly fitted from the data (as per Equation (2)) as a dotted–dashed line, and that derived from the GSMF as per Equation (5) as a solid line. We find that the two determinations of the cosmic SFR density are in rather good agreement up to redshift $z \sim 2$. At $z > 2$ the integration of the SFRF directly fitted from the data yields a larger cosmic SFR density, with the maximum differences being a factor of ~ 2.5 at $z \sim 4.5$. These discrepancies, even if rather small, may be due to biases and selection effects arising respectively in the chosen determination of the SFR and stellar mass functions. For example, the shape of the faint end of the GSMF at high redshift is highly uncertain; using a mass function whose shape steepens toward higher redshifts (see, e.g., Figure 3, dashed lines in Chruslinska & Nelemans 2019), drastically reduces the differences. Other factors which may produce these discrepancies are possible biases in the determination of the SFR from the UV+IR luminosity, in the shape of the main sequence, or in the relative contributions of the main sequence and starburst populations. As for the latter, in Caputi et al. (2017) and Bisigello et al. (2018), it is pointed out that the population of starburst galaxies tends to increase at $z \gtrsim 2$; taking this trend into account can reduce the differences between the two cosmic SFR densities (M. Chruslinska et al. 2021, in preparation). All in all, in Figure 2 we have shown that the two approaches yield a rather good agreement, particularly at $z \lesssim 2$, and we have quantitatively characterized the differences toward higher redshifts. For reference, in Figure 2 the classic determination of the cosmic SFR density by Madau & Dickinson (2014) is also reported, which is seen to be a factor of ~ 2 lower than some more recent IR data.

The main advantage of an approach based on the SFRF is that it is rather direct. Indeed, the SFR is the main quantity we are interested in, since, in providing an IMF, it gives the effective number of stars formed, and so provides a normalization for the DCOs' merging rates. Starting from the SFRF we have a direct measure of the number density of galaxies with a given SFR at a certain redshift. Instead, starting from the GSMF, the computation of the SFR requires a step more, since it involves the convolution with the main sequence and a

correct modelization of the relative abundance of MS galaxies and starbursts.

On the other hand, the GSMF provides direct statistics of the stellar masses of star-forming galaxies and, as shown above, the distribution of SFRs at fixed stellar mass and redshift is well established in the literature. Therefore, once the stellar mass is known, it is easy to associate an SFR and to use a scaling relation to infer its metallicity. Contrariwise, in fixing the SFR and redshift, the association of a stellar mass is not straightforward from an empirical point of view, and some assumptions about the galaxy SFH should be made, as we will see in Section 3.1.2. It is therefore trickier to use a scaling relation to assign metallicity. Still, starting from the SFRF, it is possible to follow the chemical enrichment of a galaxy using a model of galaxy evolution, as shown in, e.g., Boco et al. (2019).

A final comparison concerns the possibility of disentangling different galactic populations using the two statistics mentioned above. From the SFRF we can determine the contribution to the total cosmic SFR density of late type disk galaxies (mainly traced by UV data) and progenitors of local early-type galaxies (mainly traced by far-IR/(sub)mm data). From the GSMF, it is possible to differentiate between MSGs and starbursts. Understanding the contribution to the total SFR and the metallicities of different galactic populations can also be important in associating a host galaxy to a GW event.

Another method commonly used in the literature to describe the SFR density per metallicity bin as a function of redshift is to combine one of the cosmic SFR determinations with a standalone metallicity distribution (see, e.g., Belczynski et al. 2016; Cao et al. 2018; Li et al. 2018). In this approach, however, the link between the properties of star-forming galaxies and their evolution is lost, and it is not easy to retrieve an accurate cosmic metallicity distribution without passing through galaxy statistics.

3. Metallicity Distribution

Along with the stellar mass and SFR, the metal content of the gas phase of the ISM (i.e., the gas-phase metallicity, Z_{gas}) is one of the key physical quantities that has to be considered in statistical galaxy evolution studies (for a review, see Maiolino & Mannucci 2019). As can be seen in Equation (1), it is also a crucial ingredient to compute the merging rates of DCOs, since many aspects of stellar and binary evolution depend on this. On a global galaxy scale, the interplay between stellar mass, SFR, and metallicity is naturally reflected by different scaling relations, which encode information on the galaxy evolutionary stage. There are different ways to parameterize Z_{gas} as a function of M_* , redshift and/or SFR: either via an MZR (e.g., Kewley & Ellison 2008; Maiolino et al. 2008; Mannucci et al. 2009; Magnelli et al. 2012; Zahid et al. 2014; Genzel et al. 2015; Sanders et al. 2020b), or an FMR (e.g., Mannucci et al. 2010, 2011; Hunt et al. 2016; Curti et al. 2020).

The MZR is a correlation between Z_{gas} (typically measured from strong optical oxygen nebular emission lines as $12 + \log(\text{O}/\text{H})$) and M_* , and is observationally found to be valid for objects with an M_* spanning over 5 orders of magnitude. In general, at fixed M_* the MZR predicts a decline in Z_{gas} toward higher redshifts, and the level of redshift evolution is actively debated (Onodera et al. 2016; Sanders et al. 2020b). Some earlier works (e.g., Maiolino et al. 2008; Mannucci et al. 2009; Magnelli et al. 2012) found a slow evolution of the MZR out to

$z \sim 2$, but a very sharp decline in Z_{gas} of about 0.4–0.5 dex between $z = 2.5$ and $z = 3.5$, suggesting a huge drop in Z_{gas} in the early universe, and creating some tensions with modern cosmological simulations of massive galaxy formation (e.g., Davé et al. 2017; Torrey et al. 2018). The problem of accurately determining Z_{gas} becomes pronounced for high- z ($z > 3$) massive, dusty galaxies (see, e.g., discussions in Tan et al. 2014; Liu et al. 2019; Tacconi et al. 2020), where the MZR should be extrapolated. Indeed, if a linear extrapolation of a sharply declining MZR is performed, very low values of metallicity ($12 + \log(\text{O}/\text{H}) < 8.0$) are found at $z > 3$ even for massive systems.

The FMR, in contrast, is a three-parameter relation of M_* , SFR, and Z_{gas} . The inclusion of SFR takes account of the secondary dependence of metallicity on SFR initially observed in local SDSS galaxies (Mannucci et al. 2010), where Z_{gas} decreases, increasing SFR at fixed M_* . This dependence has been also confirmed over larger data sets: galaxies with the same stellar mass at the same redshift can have different metallicities due to their different SFR, showing a clear anti-correlation between Z_{gas} and sSFR (see, e.g., Hunt et al. 2016). The FMR is thought to be almost redshift-independent, as confirmed by observations out to $z \sim 3.5$ (Mannucci et al. 2010; Hunt et al. 2016). Indeed, z is not a parameter directly entering into the relation, and metallicity evolution with redshift at fixed stellar mass can be traced back to the redshift evolution of the SFR (or sSFR), described by the main sequence. Therefore the extrapolation of the FMR at $z > 3.5$ can be undertaken following the redshift evolution of the main sequence, which is determined out to $z \sim 6$. This results in a rather shallow decline of metallicity with redshift.

Thus, while the level of redshift evolution for FMR and MZR at $z \lesssim 2$ is somewhat comparable, the evolution of the two relations becomes completely different at $z \gtrsim 3$. To explicitly show these differences, we put the two relations on the same ground, computing a kind of averaged MZR from the FMR. We do this, at fixed stellar mass and redshift, averaging the metallicity given by the FMR over the distribution of SFRs around the MS in Equation (4):

$$\langle Z_{\text{MZR}} \rangle(z, M_*) = \int d \log \psi \frac{d p}{d \log \psi}(\psi|z, M_*) Z_{\text{FMR}}(M_*, \psi). \quad (6)$$

In Figure 3 we show this averaged MZR (solid lines), computed based on the FMR in Mannucci et al. (2011), which provides an updated version of the FMR presented in Mannucci et al. (2010) for lower mass galaxies. In the Figure, for comparison, we also include the MZR of Mannucci et al. (2009) (dashed lines), linearly extrapolated at $z > 3.5$. It should be noted that, while at low redshifts ($z \lesssim 2$) the two relations give comparable results, at high redshifts ($z \gtrsim 3$) the MZR evolution is very rapid, yielding values of metallicity much lower than those obtained from the FMR.

Attempting to resolve this tension is crucial, since, as shown in Section 2, the amount of SFR is not negligible at $z > 3$. However, the quest is rather challenging, since on the one hand, optical/near-IR spectroscopy suffers from large dust attenuation, and on the other hand, the statistics of sources spectroscopically studied through fine structure lines via ALMA are still limited (Boogaard et al. 2019).

Nonetheless, very recent studies have achieved great agreement between FMR and smoothly evolving MZR. Sanders et al. (2020a)

retrieved MOSDEF spectroscopy of a large sample of massive galaxies at $z > 3$, and significantly improved on the statistics of past studies over the same redshift range. By employing a novel dust-correction method, they found a much slower evolution of MZR, observing a very shallow metallicity decline of only 0.11 dex between $2.5 < z < 3.5$. This result greatly supports the FMR and slowly evolving MZRs calibrated from UV+IR data (Genzel et al. 2015).

On top of this, important evidence of a significant metal enrichment in the early universe has come from novel dust mass (M_{dust}) estimates in distant galaxies at $z > 3 - 6$ (e.g., da Cunha et al. 2015; Donevski et al. 2020; Ginolfi et al. 2020). For instance, by analyzing a large sample of 300 massive ($M_* > 10^{10} M_\odot$) dusty galaxies in the COSMOS field, observed by ALMA over a wide redshift range ($0.5 < z < 5.25$), Donevski et al. 2020 show that, in order to explain the observed M_{dust} , their Z_{gas} are, on average, close to solar ($12 + \log(\text{O}/\text{H}) = 8.64$ and $12 + \log(\text{O}/\text{H}) = 8.52$ for MS and SB galaxies, respectively). These values are in great agreement with recent direct Z_{gas} measurements via the $[\text{NII}]\lambda 6584/\text{H}\alpha$ ratio by Shapley et al. (2020) for dusty galaxies within the same mass range at $z \sim 2$.

All of the above complements classical arguments from stellar archeology, suggesting a fast metal enrichment of galaxies even at high z . Indeed, the study of stellar emission in local massive early-type galaxies can place very good constraints on their metallicity evolution: stars observed in these galaxies, formed typically at high redshifts, are found to be almost coeval and α -enhanced, indicating a short (< 1 Gyr) burst of high star formation, stopped by some form of energetic feedback (e.g., Romano et al. 2002; Thomas et al. 2005, 2010; Gallazzi et al. 2006; Johansson et al. 2012). Their stellar metallicity ranges from $0.5 Z_\odot - 2 Z_\odot$ (see Thomas et al. 2010; Gallazzi et al. 2014; Maiolino & Mannucci 2019), implying that their chemical enrichment should have been rather rapid. In Morishita et al. 2019, a sample of 24 quiescent galaxies at $z \sim 2$ was studied, finding average stellar metallicities of $Z \sim 1.5 - 2 Z_\odot$ (see also Saracco et al. 2020); in particular, the authors find that the relation between the stellar mass and stellar metallicity of their sample shows no evolution with respect to the same relation for $z \sim 0$ galaxies in Gallazzi et al. (2014). Finally, a direct measure of metallicity through the $[\text{O III}]\lambda_{88 \mu\text{m}}/[\text{N II}]\lambda_{122 \mu\text{m}}$ line ratio in high redshift quasar hosts (up to $z \sim 7.5$) has been performed by several authors, showing solar and supersolar metallicity values with no signs of redshift evolution (see, e.g., Juarez et al. 2009; Novak et al. 2019; Li et al. 2020; Onoue et al. 2020).

These numerous findings point toward the need for rapid metal enrichment in the distant universe, a scenario that has recently been proposed theoretically by several authors (Asano et al. 2013; Bethermin et al. 2015; Popping et al. 2017; Pantoni et al. 2019; Vijayan et al. 2019; Lapi et al. 2020). We have also explored predictions regarding metallicity evolution from state-of-the-art cosmological simulations (Davé et al. 2019) that self-consistently model gas and dust under standard IMF. By looking at different snapshots over the redshift range $0 < z < 5$ for the most massive objects ($10^{10} M_\odot < M_* < 10^{11} M_\odot$) we found a very shallow Z_{gas} evolution of only 0.3 dex drop from $z \sim 0$ to $z \sim 5$. This further strengthens the observational findings cited above, which may suffer from selection bias.

Evidence for substantial metal content is also found for less massive galaxies ($10^9 < M_* < 10^{9.5} M_\odot$) in the epoch of re-ionization ($6 < z < 9$, Jones et al. 2020; Strait et al. 2020).

These studies claim that the observed Z_{gas} can be achieved by extrapolating FMR or slowly evolving MZRs.

All these reasons motivate us to apply prescriptions based on FMR as a main scaling relation to infer the metal properties of galaxies at high z 's (see the next Section). However, given the substantial uncertainties, in Section 3.2 we also show the case in which an MZR with a rapid decrease in Z_{gas} with redshift (e.g., Mannucci et al. 2009) is assumed as representative for the whole population of galaxies at $z > 3$.

3.1. The Galactic Term Computed through an FMR

Given all the arguments above, we compute the galactic term $d\dot{M}_{\text{SFR}}/dV dZ$ using the FMR presented in Mannucci et al. (2011), assuming that we can extrapolate the FMR in the same form even at $z > 3.5$, as noted in Section 3. Since the FMR is a relation between stellar mass, SFR, and metallicity ($Z_{\text{FMR}} = Z_{\text{FMR}}(M_*, \psi)$) we can use both the GSMF (Section 3.1.1) and the SFRF (Section 3.1.2) as galaxy statistics to perform the computation.

3.1.1. GSMF + FMR

Fixing redshift and stellar mass, we can derive a distribution in SFR as given in Equation (4); therefore the factor $d\dot{M}_{\text{SFR}}/dV dZ$ can be computed as:

$$\begin{aligned} \frac{d\dot{M}_{\text{SFR}}}{dV dZ}(Z|z) &= \int d\log M_* \frac{dN}{dV d\log M_*}(\log M_*|z) \\ &\times \int d\log \psi \psi \frac{dp}{d\log \psi}(\psi|z, M_*) \\ &\times \left. \frac{dp}{dZ} \right|_{\text{FMR}}(Z|Z_{\text{FMR}}(M_*, \psi)) \end{aligned} \quad (7)$$

where $dp/d\log Z|_{\text{FMR}}(Z|Z_{\text{FMR}}(M_*, \psi)) \propto \exp[-(\log Z - \log Z_{\text{FMR}}(M_*, \psi))^2 / 2\sigma_{\text{FMR}}^2]$ is just a log-normal distribution around the logarithmic metallicity value set by the FMR at fixed stellar mass and SFR, the factor $dN/dV d\log M_*$ represents the GSMF, and the factor $dp/d\log \psi$ is the distribution in SFR around the MS, computed as in Equation (4). Note that, using the FMR, there is not an explicit redshift dependence on the value of the metallicity; the redshift dependence arises only indirectly via the GSMF and the distribution of SFR $dp/d\log \psi$ around the MS value.

In Figure 4 (top panel), we show the result of Equation (7), using the Mannucci et al. (2011) FMR, and the GSMF from Chruslinska & Nelemans (2019). The redshift dependence of the cosmic SFR density reflects the black solid line in Figure 2, as expected, since the GSMF is used as starting point. As for the metallicity dependence, we note that its redshift evolution is very mild: there is no net evidence of a strong decrease with redshift of the metallicity at which star formation occurs, as expected looking at Figure 3. In fact, while at $z \lesssim 2$, most of the star formation takes place at around solar values, at $z \sim 4 - 5$ the typical values of the metallicity at which star formation occurs are around $Z \sim 0.4 - 0.5 Z_\odot$. The bottom left and bottom right panels show, respectively, the contribution of MSGs and starbursts. It can be observed that the metallicity at which starbursts form stars tends to be slightly lower. This is natural, since, at fixed mass, the FMR predicts lower metallicities, increasing the SFR.

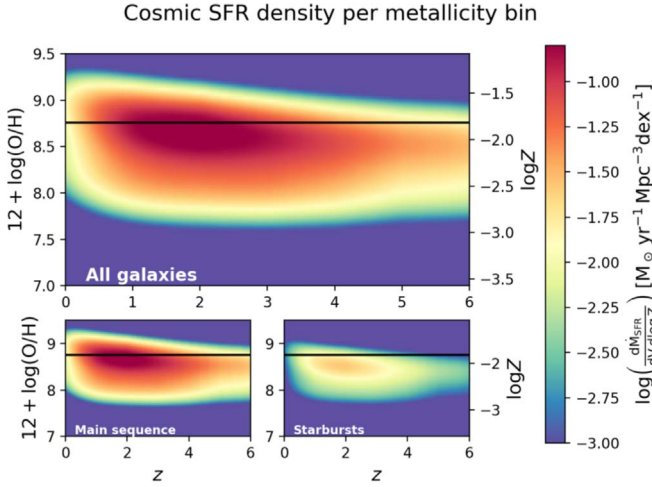


Figure 4. Top panel: the factor $\log(d\dot{M}_{\text{SFR}}/dV d \log Z)$, computed by convolving the GSMF with the FMR of Mannucci et al. (2011) (color coded) as a function of redshift on the x -axis and gas-phase metallicity $12 + \log(\text{O}/\text{H})$ on the left y -axis; on the right y -axis the logarithm of the metallicity $\log Z$ is plotted, and the solar value is plotted as a black solid line. Bottom left panel: the contribution to cosmic SFR density from main sequence galaxies. Bottom right panel: the contribution to cosmic SFR density from starburst galaxies.

3.1.2. SFRF + FMR

The FMR can be used to assign metallicities even if the SFRF are chosen as galaxy statistics. The main difficulty is that whereas at fixed redshift and stellar mass we are able to construct a distribution of SFRs, it is not clear how to derive a distribution of galaxies stellar masses at fixed redshift and SFR; there are no works in the literature which examine the issue of deriving a stellar mass distribution from empirical data. This is why, in order to roughly estimate such stellar mass distribution, we must assume an SFH for our galaxies.

Since we are considering only star-forming galaxies, the value of masses that can be assumed at fixed redshift and SFR is less than or equal to the value of mass given by the main sequence $M_{\star, \text{MS}}(z, \psi)$; all the values of mass larger than this represent quenched galaxies which are no longer forming stars. In fact, we will not sharply cut all the stellar masses above $M_{\star, \text{MS}}$, instead, we insert a Gaussian tail for masses $M_{\star} \geq M_{\star, \text{MS}}$. In terms of the mass distribution for stellar masses smaller than the MS mass ($M_{\star} < M_{\star, \text{MS}}$), we should make some assumptions regarding the galaxies' SFH.

For ETG progenitor galaxies, SED modeling studies (e.g., Papovich et al. 2011; Smit et al. 2012; Moustakas et al. 2013; Steinhardt et al. 2014; Cassara et al. 2016; Citro et al. 2016) suggest that the SFH can be described with a truncated power-law shape, rising with a shallow slope ≤ 0.5 over a quite short star formation timescale $\leq 1 \text{Gyr}$. On the other hand, late type disk dominated galaxies tend to have, on average, an SFH which declines exponentially over rather long star formation timescales $\tau_{\psi} \sim$ several Gyr (see Chiappini et al. 1997; Courteau et al. 2014; Pezzulli & Fraternali 2016; Grisoni et al. 2017; Lapi et al. 2020). Even if the star formation timescales are very different, the SFRs in both cases are nearly constant with time: for ETG progenitors, the SFR range is not larger than a factor of ~ 1.5 for most of their lifetime, while for LTGs the SFR changes only by a factor of ~ 2.5 over $\sim 8\text{--}9 \text{Gyr}$. For this reason, for the sake of simplicity, we assume a constant SFH for the galaxies considered in this work. Under this assumption, the stellar mass of a galaxy increases linearly with time, with a slope set by its SFR. The

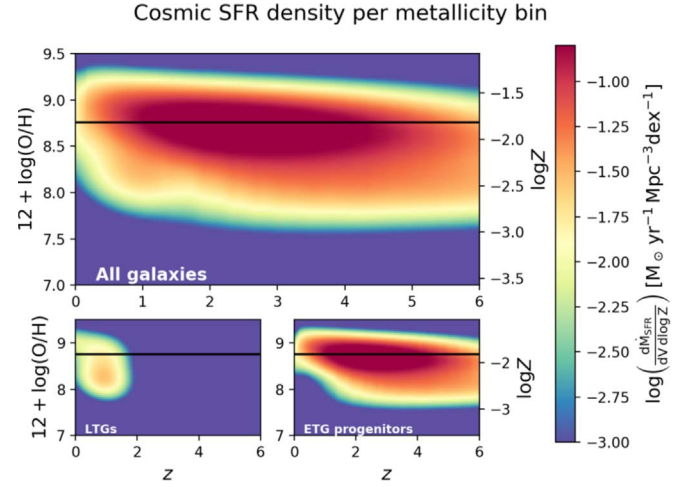


Figure 5. Top panel: the factor $\log(d\dot{M}_{\text{SFR}}/dV d \log Z)$, computed by convolving the SFRF with the FMR of Mannucci et al. (2011) (color coded) as a function of redshift on the x -axis and gas-phase metallicity $12 + \log(\text{O}/\text{H})$ on the left y -axis; on the right y -axis the logarithm of the metallicity $\log Z$ is plotted, and the solar value is plotted as a black solid line. Bottom left panel: contribution to the cosmic SFR density from LTGs. Bottom right panel: contribution to the cosmic SFR density from ETG progenitors.

logarithmic distribution of masses, at fixed redshift and SFR, is therefore proportional to the mass itself and can be written as:

$$\frac{dp}{d \log M_{\star}}(M_{\star}|z, \psi) \propto \begin{cases} M_{\star} & M_{\star} < M_{\star, \text{MS}} \\ M_{\star, \text{MS}} \times \exp\left(-\frac{(\log M_{\star} - \log M_{\star, \text{MS}})^2}{2\sigma_{M_{\star}}^2}\right) & M_{\star} \geq M_{\star, \text{MS}} \end{cases} \quad (8)$$

normalized to unity. Actually, this is a crude approximation of what was achieved in Mancuso et al. (2016b), where the authors show how to reproduce an MS with similar prescriptions.

Using the SFRF as a starting point, and the distribution in Equation (8) as stellar mass distribution at given z and ψ , we can assign a metallicity to galaxies with the FMR and compute the factor $d\dot{M}_{\text{SFR}}/dV dZ$ as:

$$\frac{d\dot{M}_{\text{SFR}}}{dV dZ}(Z|z) = \int d \log \psi \psi \frac{dN}{dV d \log \psi} \int dM_{\star} \times \frac{dp}{dM_{\star}}(M_{\star}|z, \psi) \frac{dp}{dZ} \Big|_{\text{FMR}}(Z|Z_{\text{FMR}}(M_{\star}, \psi)) \quad (9)$$

where $dp/d \log Z|_{\text{FMR}}(Z|Z_{\text{FMR}}(M_{\star}, \psi)) \propto \exp[-(\log Z - \log Z_{\text{FMR}}(M_{\star}, \psi))^2 / 2\sigma_{\text{FMR}}^2]$ is the same log-normal distribution around the central logarithmic value of metallicity set by the FMR as appears in Equation (7).

The result of the computation in Equation (9) is shown in Figure 5. It can be observed that the redshift dependence of the SFR density reflects the shape of the cosmic SFR density derived by the integration of the SFRF (dotted–dashed lines in Figure 2), with a broader peak slightly shifted toward $z \sim 2.5\text{--}3$, as expected, since the employed galaxy statistics are the same. The metallicity dependence on redshift is similar to that in Figure 4, since they share the same prescription to assign metallicity (the FMR). In particular, the redshift decrease is also mild in this case, with most of the star formation occurring at solar metallicities for $z \lesssim 2$ and at $Z \sim 0.4\text{--}0.5 Z_{\odot}$ for $z \sim 4\text{--}5$. In a case where the SFRFs are used as a starting point, it is more difficult to disentangle the

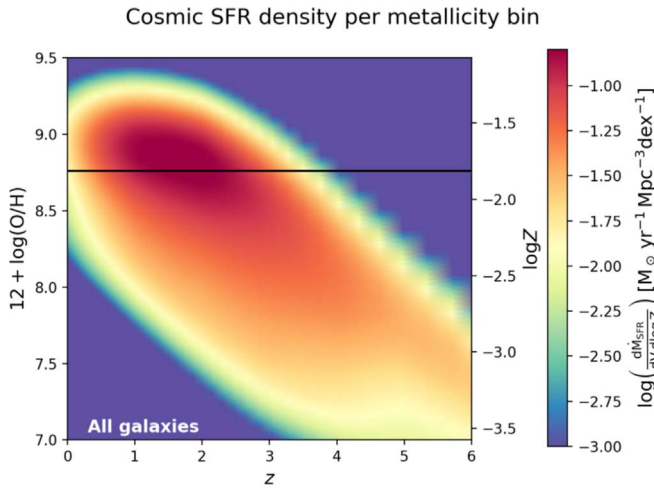


Figure 6. The factor $\log(dM_{\text{SFR}}/dV d \log Z)$ computed by convolving the GSMF with the MZR of Mannucci et al. (2009) (color coded) as a function of redshift on the x -axis and gas-phase metallicity $12 + \log(\text{O}/\text{H})$ on the left y -axis; on the right y -axis the logarithm of the metallicity $\log Z$ is plotted, and the solar value is plotted as a black solid line.

contribution of MSGs with respect to starbursts. On the other hand, it is easier to look at the contribution to the total SFR density given by LTGs and ETG progenitors, as explained in Section 2. These contributions are shown, respectively, in the bottom left and bottom right panels of Figure 5. It can be seen that LTGs, having on average a lower stellar mass, tend to produce a tail of lower metallicity star formation even at low redshift. However, the bulk of the SFR density occurs at $z \gtrsim 1$, and it is given by ETG progenitors.

3.2. The Galactic Term Computed through an MZR

In Section 3.1 we computed the galactic term using an FMR which, as shown in our results, implies a shallow decrease in metallicity with redshift. We now compute the same factor, $dM_{\text{SFR}}/dV dZ$, using instead a sharply declining MZR (Mannucci et al. 2009), linearly extrapolated at $z > 3.5$, to see how much this choice will impact on the final results.

The factor $dM_{\text{SFR}}/dV dZ$ can be computed by convolving the MZR with the stellar GSMF at a given redshift, and using the distribution around the main sequence to assign an SFR to a galaxy with a given stellar mass and redshift:

$$\begin{aligned} \frac{dM_{\text{SFR}}}{dV dZ}(Z|z) &= \int d \log M_{\star} \frac{dN}{dV d \log M_{\star}}(\log M_{\star}|z) \\ &\times \left. \frac{dp}{dZ} \right|_{\text{MZR}}(Z|Z_{\text{MZR}}(z, M_{\star})) \\ &\times \int d \log \psi \frac{dp}{d \log \psi}(\psi|z, M_{\star}) \psi \end{aligned} \quad (10)$$

where $dp/d \log Z|_{\text{MZR}}(Z|Z_{\text{MZR}}(z, M_{\star})) \propto \exp[-(\log Z - \log Z_{\text{MZR}}(z, M_{\star}))^2 / 2\sigma_{\text{MZR}}^2]$ is a log-normal distribution around the logarithmic value given by the MZR ($\log Z_{\text{MZR}}$).

In Figure 6 we show the resulting $dM_{\text{SFR}}/dV dZ$ (color code) as a function of redshift and metallicity. The redshift dependence of the cosmic SFR reflects the shape presented in Figure 2 (solid lines), obtained using the GSMF as galaxy statistic, with a peak of star formation around $z \sim 2$. As for the metallicity dependence, at lower redshifts, $z \lesssim 2$, the metallicity stays rather high, similarly to

the FMR cases, with most of the star formation occurring at slightly supersolar values, while at higher z the metallicity starts to decline rapidly, with most of the star formation occurring at $Z \leq 0.1 Z_{\odot}$ at $z \gtrsim 4$, in contrast to the FMR cases, in which the metallicity stays around $\sim 0.4 Z_{\odot}$, reaching values of only $\sim 0.1 Z_{\odot}$ in the less massive systems. We stress that the differences between the two approaches are rather small at low redshifts $z \leq 2.5$ and start to be significant at higher redshifts, mainly in the regions where both relations have been extrapolated. The main message here is that extrapolating the FMR, which is a redshift-independent relation, can yield higher metallicity values with respect to a sharply declining MZR, more in agreement with the arguments discussed at the beginning of this section.

4. Merging Rates of Compact Binaries

In this Section we show how the different galactic terms, $dM_{\text{SFR}}/dV dZ$, computed above impact on the merging rates and the properties of merging compact binaries. The three cases for which the galactic term has been computed are: stellar mass functions as galaxy statistics with the FMR to assign metallicity (GSMF+FMR case, Equation (7)), the SFRF as statistics with the FMR to assign metallicity (SFRF+FMR, Equation (9)), and the stellar mass function as statistics with the MZR to assign metallicity (GSMF+MZR, Equation (10)).

However, to compute the merging rates (Equation (1)) we need not only the galactic term, $dM_{\text{SFR}}/dV dZ$, discussed throughout the paper, but also the term $dN/dM_{\text{SFR}} dM dt_d$, depending on stellar and binary evolution, counting the number of merging events per units of star formed mass, chirp mass, and time delay. In Section 4.1 we describe the choices made to compute this term and then, in Section 4.2, we derive the merging rates for the three types of compact binaries: BH–BH, NS–NS and BH–NS. Finally, in Section 4.3 we discuss the time delay between the formation of the binary and the merger, which will give us information on the typical ages of the stellar population of the galaxy hosting the merging event.

A general caveat for this Section is that, while we compare the results arising from the usage of different galactic terms $dM_{\text{SFR}}/dV dZ$, the merging rates could be strongly affected by the modelization of the factor $dN/dM_{\text{SFR}} dM dt_d$, as we will see in Section 4.1. As such, the presented merging rates should not be interpreted as an exact determination, but simply as the results of the different galactic prescriptions applied to a specific reference case for the stellar term $dN/dM_{\text{SFR}} dM dt_d$.

4.1. The Stellar Term

Within the isolated binary evolution scenario leading to the formation of merging DCOs (such as those considered in this paper), the stellar term appearing in Equation (1) is commonly obtained from binary population synthesis simulations (e.g., Belczynski et al. 2016; Eldridge et al. 2017; Mapelli et al. 2017; Stevenson et al. 2017). The outcome of these simulations (and therefore also the stellar term) depends on a number of assumptions made in order to describe the evolution of massive stars and binary interactions. Many of these are highly uncertain (e.g., common envelope evolution, core-collapse physics and the related natal kicks), and are known to strongly affect the properties of the simulated populations of merging DCOs (e.g., Portegies Zwart & Yungelson 1998; Dominik et al. 2012; Chruslinska et al. 2018). Stellar evolution depends on

metallicity — it affects, for instance, stellar winds and radii, also impacting the nature and outcome of binary interactions (e.g., Maeder 1992; Hurley et al. 2000; Vink et al. 2001; Belczynski et al. 2010a). As a consequence, the resulting stellar term also depends on metallicity.

This term can be separated into three main factors:

$$\frac{dN}{dM_{\text{SFR}} d\mathcal{M} dt_d}(Z) = \frac{dN}{dM_{\text{SFR}}}(Z) \times \frac{dp}{d\mathcal{M}}(Z) \times \frac{dp}{dt_d} \quad (11)$$

where dN/dM_{SFR} is the number of merging DCOs formed per unit of mass formed in stars (formation efficiency) at metallicity Z , $dp/d\mathcal{M}$ is the metallicity-dependent chirp mass distribution, and dp/dt_d is the distribution of delay times between the formation of the progenitor binary and the DCO merger.

The delay time distribution resulting from binary population synthesis is commonly found to be well described by a simple inverse proportionality, $dp/dt_d \propto t_d^{-1}$, independent of the DCO type or metallicity. We assume $dp/dt_d \propto t_d^{-1}$ with the minimum $t_{d,\text{min}} = 50$ Myr. The distribution is normalized to unity between $t_{d,\text{min}}$ and the age of the universe.

We base the remaining two factors on the results of population synthesis calculations, using the model “reference B” from Chruslinska et al. (2018).⁷ We note that this is just an example. The exact results concerning the populations of merging DCOs presented later in this section would generally be affected by the choice of the population synthesis model (e.g., Chruslinska et al. 2019). However, the main focus of this work is on the galactic term, and a more in-depth discussion of the uncertainties relating to binary evolution is beyond the scope of this study.

Formation efficiency as a function of metallicity for the chosen evolutionary model is shown in Chruslinska et al. (2019) (Figure 1, thin lines). The formation efficiency of merging BH–BH is typically found to show a strong low metallicity preference (e.g., Belczynski et al. 2010b; Dominik et al. 2012; Eldridge & Stanway 2016; Stevenson et al. 2017; Klencki et al. 2018; Giacobbo et al. 2018). This dependence is also present in the chosen model, with BH–BH formation efficiency dropping by almost two orders of magnitude between $0.2 Z_{\odot}$ and $0.4 Z_{\odot}$. This dependence is generally weaker for other DCO types, and in the adopted model shows a factor of $\lesssim 10$ increase/decrease toward high metallicity for NS–NS/BH–NS.

The metallicity dependence of the chirp mass distribution is to large extent a consequence of the metallicity dependence of the maximum mass of the stellar remnant resulting from single stellar evolution. Due to metallicity-dependent line-driven wind mass loss rates of massive stars (e.g., Vink et al. 2001; Vink & de Koter 2005; Sundqvist et al. 2019; Sander et al. 2020), a star with the same initial mass leaves a more massive stellar remnant at lower metallicity. As a result, a population of DCOs containing a higher fraction of objects originating from low metallicity progenitors will result in a chirp mass distribution with a more extended high mass tail (see, e.g., Figure 4 in Chruslinska et al. 2019).

⁷ We use the simulation data publicly available under this URL: <https://www.syntheticuniverse.org/>.

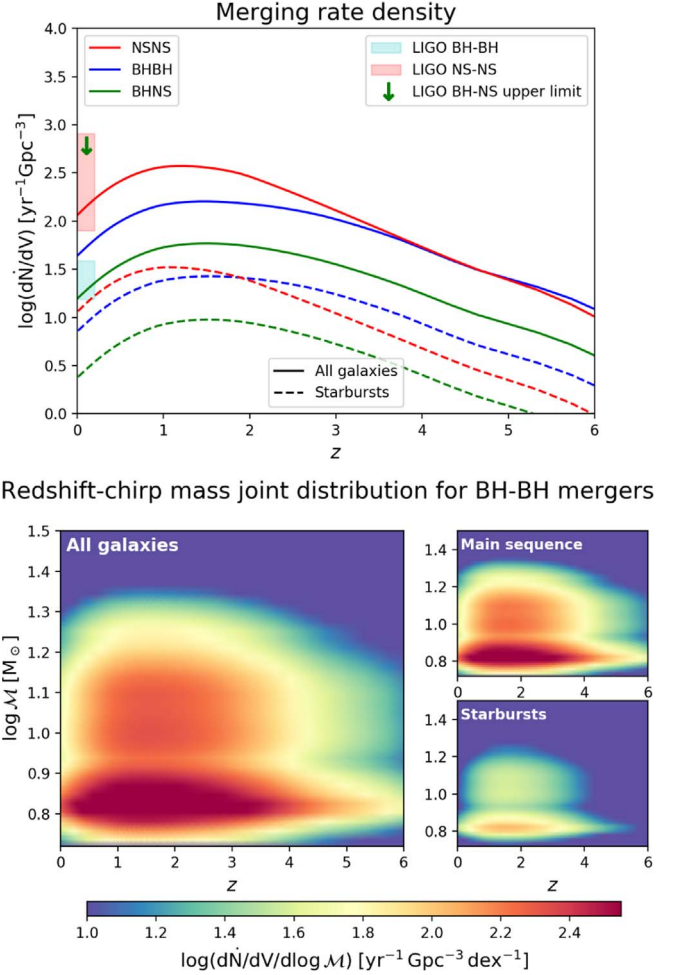


Figure 7. Top panel: merger rate density of double compact object binaries as a function of redshift, computed using the GSMF as galaxy statistics and the FMR, following Equation (7). Blue lines refer to BH–BH, red lines to NS–NS, green lines to BH–NS events. Solid lines represent the merging happening in all the galaxies (main sequence and starbursts), while the dashed lines highlight the contribution of starbursts. The red and blue patches and the green arrow at $z \sim 0$ represent the LIGO/Virgo 90% confidence intervals on the local rates for NS–NS and BH–BH and the upper limit for BH–NS after the O1, O2 and first half of O3 runs (Abbott et al. 2019, 2020b). Bottom panels: differential merging rates $\log(d\dot{N}/dV d \log \mathcal{M})$ for the BH–BH case (color code) as a function of redshift and chirp mass. Contributions from all the galaxies (left panel), from main sequence galaxies (top right panel) and starbursts (bottom right panel).

4.2. Merging Rates Computation

The merging rates per chirp mass units are computed as in Equation (1); performing a further integration over the chirp mass, we get the redshift distribution of the merging rate density for the three types of merging binaries: BH–BH, NS–NS and BH–NS. In Figures 7, 8 and 9 we show, respectively, the results for the three different ways to compute the galactic term described in this paper: GSMF+FMR (Equation (7)), SFRF+FMR (Equation (9)) and GSMF+MZR (Equation (10)).

In the top panels are plotted, the merging rates redshift distributions, highlighting the contribution of starburst galaxies in the GSMF+FMR case, and the contribution of LTGs in the SFRF+FMR case. The local ($z \sim 0$) merging rates determinations by LIGO/Virgo for BH–BH ($15.3\text{--}38.8 \text{ Gpc}^{-3} \text{ yr}^{-1}$), NS–NS ($80\text{--}810 \text{ Gpc}^{-3} \text{ yr}^{-1}$) and BH–NS ($\leq 610 \text{ Gpc}^{-3} \text{ yr}^{-1}$) are also reported (see Abbott et al. 2019, 2020b). The NS–NS

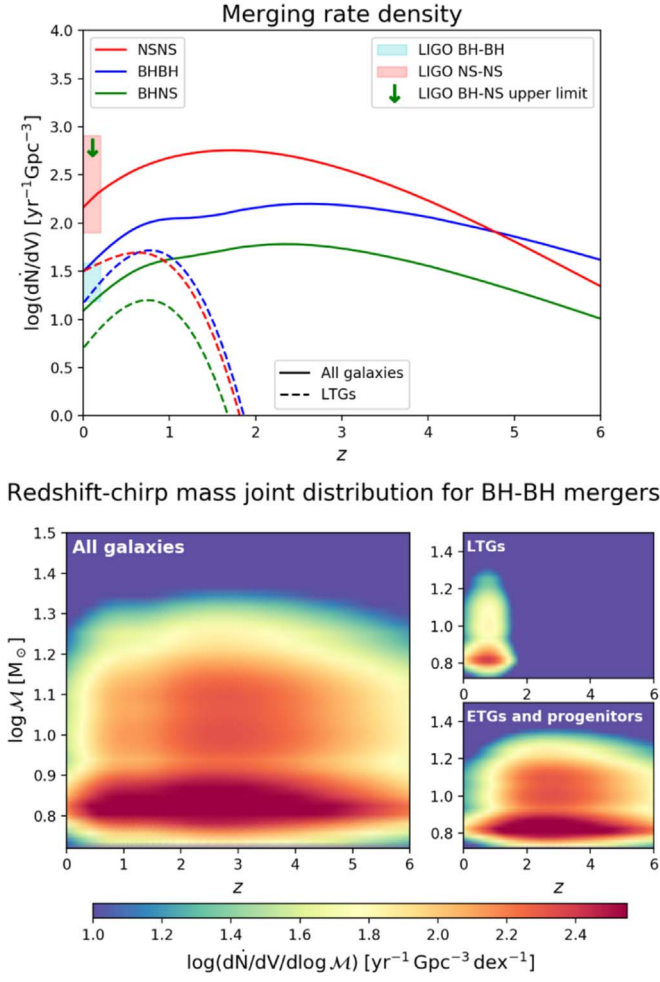


Figure 8. Top panel: merger rate density of double compact object binaries as a function of redshift, computed using the SFRF as galaxy statistics and the FMR, following Equation (9). Blue lines refer to BH–BH, red lines to NS–NS, green lines to BH–NS events. Solid lines represent the merging happening in all the galaxies (LTGs, ETGs, and their progenitors), while the dashed lines highlight the contribution of LTGs. The red and blue patches and the green arrow at $z \sim 0$ represent the LIGO/Virgo 90% confidence intervals on the local rates for NS–NS and BH–BH and the upper limit for BH–NS after the O1, O2, and first half of O3 runs (Abbott et al. 2019, 2020b). Bottom panels: differential merging rates $\log(dN/dV d \log \mathcal{M})$ for the BH–BH case (color code) as a function of redshift and chirp mass. Contribution from all the galaxies (left panel), from LTGs (top right panel) and ETGs and their progenitors (bottom right panel).

and BH–NS merging rates fall inside the LIGO/Virgo interval for all the 3 cases considered, the BH–BH merging rates are slightly above the LIGO/Virgo interval for the GSMF+FMR and GSMF+MZR cases, while they fall within it in the SFRF+FMR case.⁸ Comparing the top panels of Figures 7 and 9, referring to the GSMF+FMR and GSMF+MZR cases, which use the same galaxy statistics as a starting point (GSMF) and differ only in the metallicity prescriptions, we notice that the merging rates of NS–NS and BH–NS are similar, since they are less dependent on metallicity. On the other hand, the BH–BH merging rates, which are strongly dependent on metallicity, are

⁸ We stress again that the agreement/disagreement with the LIGO/Virgo determinations may be due to the modelization of the stellar term. Moreover, this is only one of the many constraints that a galactic or stellar model should be able to satisfy. As such, the local rate alone does not represent a proof of the goodness of a model with respect to the others.

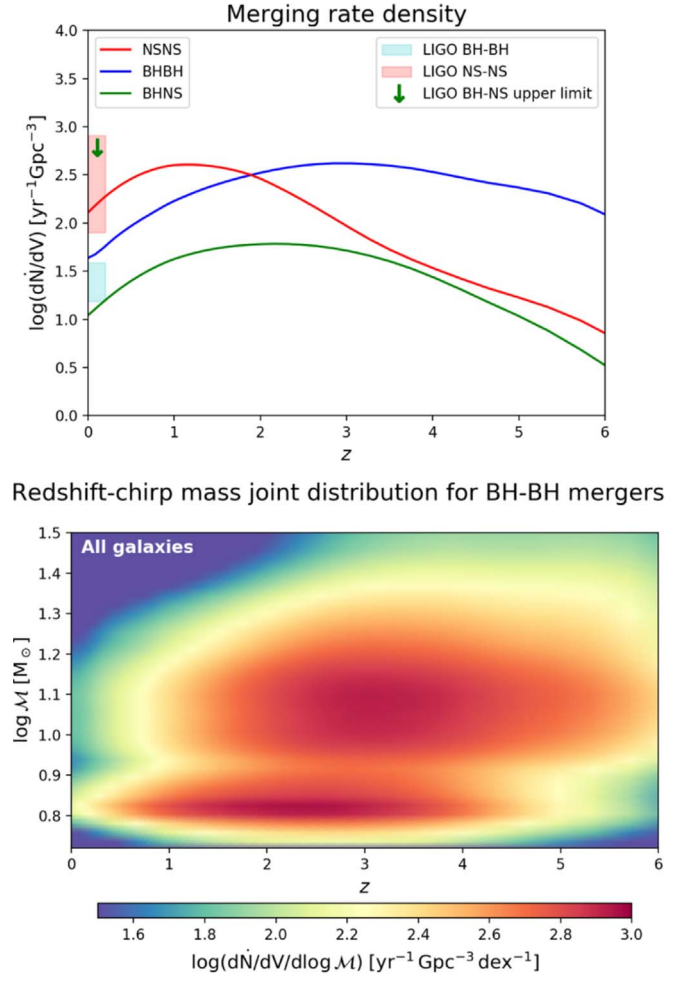


Figure 9. Top panel: merger rate density of double compact object binaries as a function of redshift, computed using the GSMF as galaxy statistics and the MZR, following Equation (10). Blue lines refer to BH–BH, red lines to NS–NS, green lines to BH–NS events. The red and blue patches and the green arrow at $z \sim 0$ represent the LIGO/Virgo 90% confidence intervals on the local rates for NS–NS and BH–BH and the upper limit for BH–NS after the O1, O2, and first half of O3 runs (Abbott et al. 2019, 2020b). Bottom panel: differential merging rate $\log(dN/dV d \log \mathcal{M})$ for the BH–BH case (color code) as a function of redshift and chirp mass. Note the change in the color code scale due to the larger number of BH–BH mergers occurring in this case.

substantially different: at low redshift ($z < 1.5$) they are similar due to the similar behavior of the metallicity distribution, while at high redshift ($z \geq 1.5$) they are larger for the MZR case (by a maximum factor of ~ 10) due to the strong decrease in metallicity at high redshift in the MZR case (see Figures 4 and 6). As for the SFRF+FMR case (Figure 8) the BH–BH merging rates lies in-between. In fact, even if the metallicity, assigned through the FMR, stays rather high, suppressing BH–BH mergers, this fact is partially compensated for by the higher cosmic SFR density at high redshift obtained when the SFRF are employed as galaxy statistics (see Figure 2). This is also reflected in the larger merging rates for NS–NS and BH–NS in the SFRF+FMR case.

The bottom panels of Figures 7–9 are also rather informative. These show the redshift and chirp mass distribution of the BH–BH merging rates. In the GSMF+MZR case (Figure 9) the chirp mass distribution extends up to $\mathcal{M} \gtrsim 30 M_{\odot}$ at high redshift ($z \geq 2$) where the metallicity tends to drop at subsolar values. This high chirp mass tail is reduced for the cases in which the FMR is

used (Figure 7 and 8), since metallicity never drops too much, even at high redshifts, producing remnants with lower masses on average. We note here that none of the three cases analyzed is able to reproduce the high chirp mass events ($\mathcal{M} \gtrsim 30 M_{\odot}$) recently observed at $z < 1$ by the LIGO/Virgo collaboration (see Abbott et al. 2020a, 2020b). This is not an issue for us, since the chirp mass distribution, as well as the total rates of DCOs mergers, are strongly dependent on the selected model of stellar and binary evolution, whose discussion falls outside the scope of this work. The comparisons shown here are useful simply in order to understand the general trend of DCO mergers for different galactic prescriptions, but are not meant to reproduce the real chirp mass distribution. However, we stress that, in the three cases shown here, events with $\mathcal{M} \gtrsim 30 M_{\odot}$ are still produced, but their rate is much less than the rate of $\mathcal{M} < 30 M_{\odot}$ events. A GW detector such as Advil/Virgo would tend to detect mainly high chirp mass events, since they produce stronger GW signals, so that the chirp mass distribution of merging DCOs may substantially be altered by selection effects. In addition, other channels of GW emission should not be excluded: dynamical formation and the merger of CO binaries (see, e.g., Boco et al. 2020), as well as primordial black holes mergers (see, e.g., Scelfo et al. 2018), could contribute to the GW detections somewhat, and change the detected chirp mass distribution.

In the small plots on the bottom right of Figures 7 and 8 we show the contribution of MSGs and starbursts, for the GSMF+FMR case (Figure 7), and the contribution of LTGs, ETGs, and their star-forming progenitors, for the SFRF+FMR case (Figure 8). Between MSGs and starbursts, no evident difference can be found, it is clear just that MSGs are the main contributors to BH–BH merging rates. This is clearly dependent on the way we chose to model starbursts: we fixed their fraction to be $\sim 3\%$ for all the stellar masses at all redshifts; it would be interesting to see how this would change were the starburst fraction to be treated in a more detailed way (see M. Chruslinska et al. 2021, in preparation). Instead, the contribution of LTGs and ETGs is substantially different: LTGs contribute to the merging rates only at low redshift ($z \leq 2$) while only ETG progenitors are present at higher redshifts. At $z \leq 2$, the relatively longer tail toward larger chirp masses in LTGs can be explained by the fact that they have, on average, lower metallicities (see Figure 5).

4.3. Chirp Mass and Time Delay

Differential merging rates as a function of chirp mass and time delay tell us how the time delays and chirp masses are distributed for the merging events. They can be very helpful even for host galaxy association, since, given the chirp mass of the signal, they give information on the average age of the stellar population producing the merger

These can be computed simply by avoiding the first integration in Equation (1):

$$\frac{d\dot{N}}{dV d\mathcal{M} dt_d}(t, t_d) = \int dZ \frac{dN}{dM_{\text{SFR}} d\mathcal{M} dt_d}(Z) \frac{d\dot{M}_{\text{SFR}}}{dV dZ}(t - t_d). \quad (12)$$

We present results for BH–BH mergers at $z \sim 0$. The results are shown in Figures 10–12 for the three different methods of computing the galactic term described in this paper: GSMF+FMR (Equation (7)), SFRF+FMR (Equation (9)) and GSMF+MZR (Equation (10)).

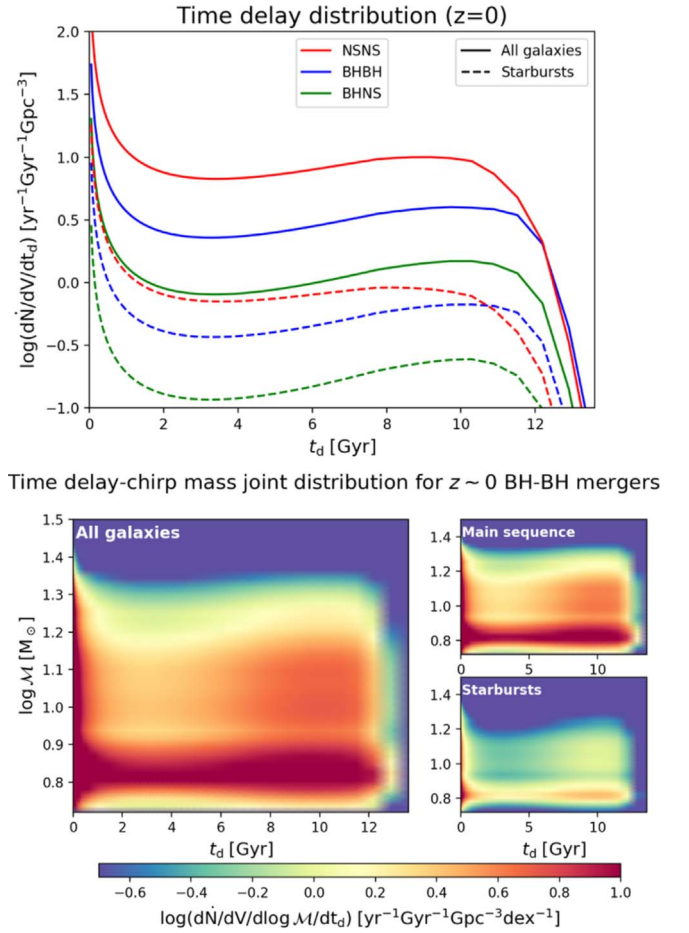


Figure 10. Top panel: differential merging rate $\log(d\dot{N}/dV dt_d)$ at $z \sim 0$ for BH–BH as a function of the time delay between the formation of the binary and the merger, computed using the GSMF for galaxy statistics and the FMR, following Equation (7). Bottom panels: differential merging rates $\log(d\dot{N}/dV d \log \mathcal{M} dt_d)$ at $z \sim 0$ for BH–BH as a function of the chirp mass and time delay. The x -axis shows the time delay, the y -axis the chirp mass, and the color code represents the logarithmic number density of merging events. Contributions from all the galaxies (left panel), from main sequence galaxies (top right panel) and starbursts (bottom right panel).

The top panels illustrate the merging rates per units of time delay $d\dot{N}/dV/dt_d$, meaning that Equation (12) has been integrated over the chirp mass. In the GSMF+FMR case we show the contribution of starburst galaxies, while in the SFRF+FMR case we show the contribution of LTGs. In all the Figures a double peak distribution is clearly visible: the peak at low delay times is due to the shape of the intrinsic time delay distribution $dp/dt_d \propto t_d^{-1}$ favoring short time delays, while the peak at $t_d \sim 10$ – 12 Gyr is due to the huge amount of star formation happening at redshift $z \sim 2$ – 3 , which compensates for the time delay distribution favoring short time delays: a small fraction of the many objects formed at $z \sim 2$ – 3 can be seen via GW emission at $z \sim 0$.

Apart from this shape shared by all three cases, there are some differences between them that we explain here. In the cases where the GSMF is used for statistics (Figures 10 and 12) the NS–NS time delay distribution is similar, since NS–NS mergers are almost independent of metallicity. The BH–BH time delay distribution is instead rather different: while for the GSMF+FMR case (Figure 10) the time delay distribution is flatter, with $\sim 48\%$ of the BH–BH merging with $t_d \leq 6$ Gyr, for the GSMF+MZR case the second peak is more pronounced,

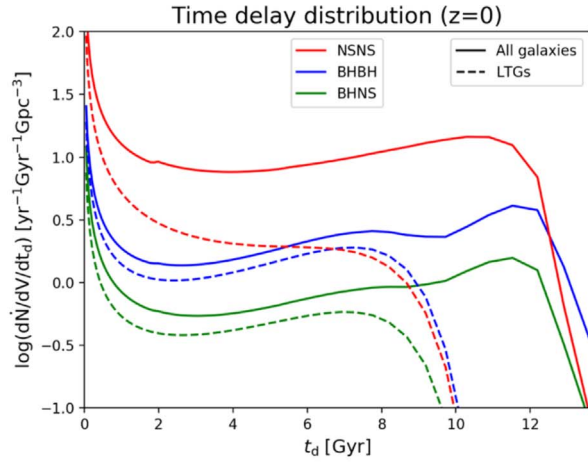
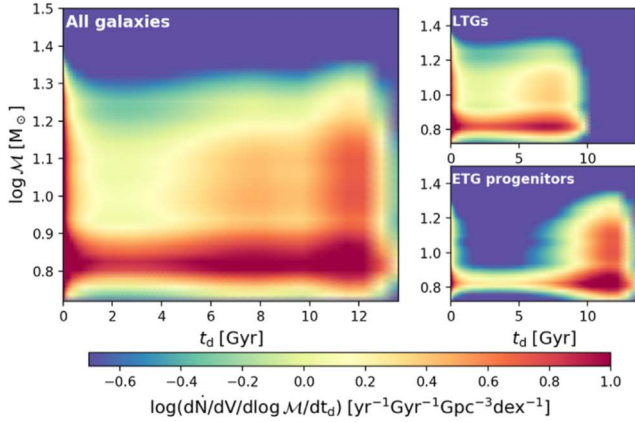
Time delay-chirp mass joint distribution for $z \sim 0$ BH-BH mergers

Figure 11. Top panel: differential merging rate $\log(d\dot{N}/dV dt_d)$ at $z \sim 0$ for BH–BH as a function of the time delay between the formation of the binary and the merger, computed using the SFRF as galaxy statistics and the FMR, following Equation (9). Bottom panels: differential merging rate $\log(d\dot{N}/dV d \log \mathcal{M} dt_d)$ at $z \sim 0$ for BH–BH as a function of chirp mass and time delay. The x -axis shows the time delay, the y -axis the chirp mass, and the color code represents the logarithmic number density of merging events. Contributions from all the galaxies (left panel), from LTGs (top right panel) and ETG progenitors (bottom right panel).

with only $\sim 20\%$ of BH–BH merging with $t_d \leq 6$ Gyr, and many events with $t_d \geq 9$ –10 Gyr. This is due to the fact that, as already shown, in the MZR case the metallicity is much lower at high redshift, increasing the contribution to the $z \sim 0$ merging events from BHs formed at high redshift. For the BH–NS mergers the same effect, if milder, can be observed. The starburst contribution, shown only in the GSMF+FMR case, is subdominant. Comparing the NS–NS and BH–BH mergers in starbursts we note a slight difference with respect to the case for all galaxies. In fact, while the NS–NS contribution is always larger than the BH–BH one in the case of all galaxies, if we restrict ourselves to starbursts, the two contributions are roughly comparable, with BH–BH events even being dominant with respect to NS–NS for $t_d > 11$ Gyr; this is due to the average lower metallicities of starbursts, which slightly enhances the occurrence of BH–BH mergers.

In the SFRF+FMR (Figure 11) case, NS–NS have a similar shape to the other cases for $t_d \leq 9$ –10 Gyr, while there is an enhancement at larger time delays, due to the higher cosmic SFR at $z \geq 2$. The contribution of LTGs to the NS–NS merging rates follows the relative abundance of LTGs with respect to ETGs with cosmic time. For the BH–BH mergers, the shape is

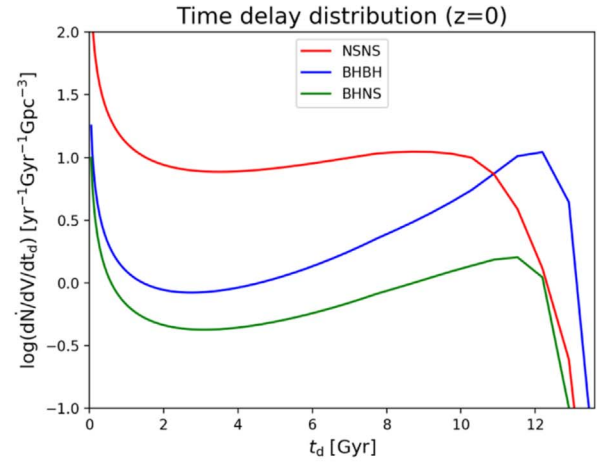
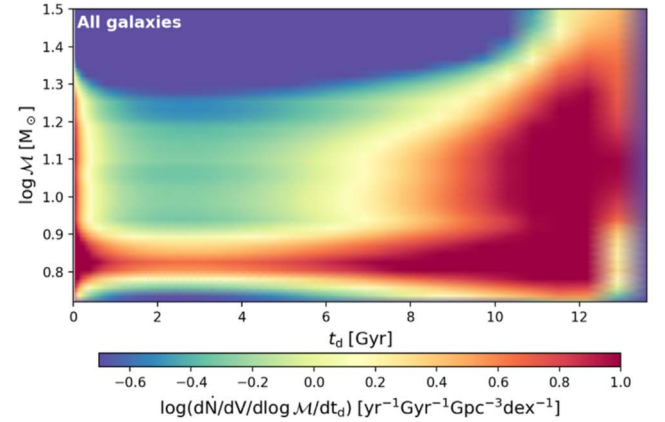
Time delay-chirp mass joint distribution for $z \sim 0$ BH-BH mergers

Figure 12. Top panel: differential merging rate $\log(d\dot{N}/dV dt_d)$ at $z \sim 0$ for BH–BH as a function of the time delay between the formation of the binary and the merger, computed using the GSMF as galaxy statistics and the MZR, following Equation (10). Bottom panel: differential merging rate $\log(d\dot{N}/dV d \log \mathcal{M} dt_d)$ at $z \sim 0$ for BH–BH as a function of chirp mass and time delay. The x -axis shows the time delay, the y -axis the chirp mass, and the color code represents the logarithmic number density of merging events.

in-between that of GSMF+FMR and GSMF+MZR: a decrease can be seen at $1 \leq t_d \leq 6$ Gyr, and a moderate enhancement at $t_d \geq 10$ Gyr, with a resulting $\sim 37\%$ of the BH–BH mergers having $t_d < 6$ Gyr. The behavior at small time delays can be explained by the rather high metallicity at low redshift, and the enhancement at high time delays is due to the larger amount of cosmic SFR, even if the metallicity remains pretty high. The contribution at low time delays comes almost exclusively from LTGs, which are less metallic, as shown in Figure 5, while events with large time delays come from ETGs forming stars at higher redshifts, producing the second peak at $t_d > 10$ Gyr.

The bottom panels also show the dependence on chirp mass. It can be seen that in the GSMF+MZR case, high chirp mass events tend to have huge time delays, while the distribution for the GSMF+FMR case is smoother. This means that in the GSMF+MZR case, the GW events at $z \sim 0$ with $\mathcal{M} \geq 20 M_\odot$ can be clearly linked to long delay times ($\gtrsim 10$ Gyr) and so to an older stellar population, while in the GSMF+FMR case the association between chirp mass and time delay is much less clear. The SFRF+FMR case lies in-between. In the bottom right small panels of Figures 10 and 11 we show, respectively, the contribution of MSGs and starbursts, and of LTGs and ETGs. Between main sequence and starburst galaxies, differences are not so evident,

due to our treatment of the starburst population, while between LTGs and ETGs the difference is huge: as already shown, the ETGs clearly contribute primarily to events with large time delays ($t_d > 9$ Gyr) and LTGs to events with $t_d < 9$ Gyr. High chirp mass events can come from both populations.

5. Conclusions

Throughout this paper we have focused on the computation of cosmic SFR density per unit metallicity ($d\dot{M}_{\text{SFR}}/dV d \log Z$) with different prescriptions for galaxy statistics and metallicity scaling relations. In particular:

1. we have shown the similarities and differences of using stellar mass functions and SFR functions as galaxy statistics, finding a good agreement between the two methods up to $z \sim 2$ and a larger cosmic SFR density at $z > 2$ if the SFR functions are employed (by a maximum factor of ~ 2.5) (see Section 2 and Figure 2). We have also discussed the main advantages and drawbacks of the two approaches: on the one hand the SFR functions provide more direct statistics relating to the SFR of galaxies. On the other hand, the GSMF can be more useful in the estimation of the galaxies' metallicities (see discussion at the end of Sections 2 and 3).
2. we have presented the two main empirical scaling relations to associate metallicities to galaxies: the MMR and the FMR. We analyzed the similarities and differences between the two relations, showing that the extrapolation of the FMR yields rather large average metallicity values ($Z \sim 0.4\text{--}0.5 Z_\odot$) even at $z > 2$, while the MZR usually implies very low metallicities ($Z < 0.1 Z_\odot$) at $z > 2$. We have detailed theoretical arguments and recent observational evidence testifying that the metallicity of high redshift dusty obscured star-forming galaxies is rather large, arguing that, in order to reproduce those metallicities, we should rely on extrapolations of the FMR or of a slowly evolving MZR (see Section 3).
3. we have combined our fiducial scaling relation (the FMR) with both of the two aforementioned types of galaxy statistics to compute the cosmic SFR density per units of metallicity ($d\dot{M}_{\text{SFR}}/dV d \log Z$) in the two cases (see Section 3 and Figures 4 and 5). We have also considered an alternative case in which a sharply evolving MZR is used, and combined it with the GSMF (see Figure 6)). We find that the differences in the employed galaxy statistics and metallicity evolution are clearly reflected in the factor $d\dot{M}_{\text{SFR}}/dV d \log Z$.

Finally, in the last section, we have chosen a stellar and binary evolution model as an example to show the effect of the different galactic terms on the merging rates and the properties of merging binaries. We find that:

1. merging rates computed using the different galactic terms are roughly consistent with the local merging rates determined by the LIGO/Virgo team (see Section 4);
2. differences in the merging rate shape are present, particularly at high redshift, where the two types of galaxy statistics and the two metallicity scaling relations differ more (see Section 4 and Figures 9, 7 and 8). In short, using the SFRF enhances the compact remnants production at $z > 2$ with respect to the GSMF case. The

metallicity relation used primarily affects the BH–BH merging rates and, in particular, the higher metallicity in the early universe (obtained via extrapolation of the FMR) hampers the BH–BH merging events by a factor of as much as ~ 10 ;

3. differences are also present in the chirp mass and time delay distributions (see Section 4 and Figures 7–12). In short, if there is little metallicity evolution with redshift, the association between the chirp mass of the GW event and the redshift at which the merging occurs is less clear than in the case in which there is a strong metallicity evolution.

However, we again remark that the results for the merging rates are also dependent on the selected stellar model, so should be interpreted simply as a case study to compare the effects of the different galactic terms.

We hope that this work on different prescriptions for galaxy statistics and metallicity can help in understanding the main properties of the merging binaries that will be detected via GWs, particularly with reference to future third generation detectors, such as the Einstein Telescope. Knowing the effects of different galactic properties on the features of the merging binaries can be extremely helpful in order to better understand star formation and galaxy evolution across cosmic time, when large-scale statistics of GW events become available. From the observational point of view, a huge boost in the characterization of galaxies' SFR and metallicity at increasingly high redshifts will come with the advent of the James Webb Space Telescope, which is suitable for measuring line diagnostics from galaxies across a broad range of redshifts, eventually in synergy with (sub)mm instruments such as ALMA.

We thank the anonymous referee for useful comments. We acknowledge financial support from the EU H2020-MSCA-ITN-2019 Project 860744 BiD4BEST: Big Data applications for black hole Evolution Studies and from the PRIN MIUR 2017 prot. 20173ML3WW 002, opening the ALMA window on the cosmic evolution of gas, stars, and massive black holes. L.B. warmly thanks Luigi Bassini, for many helpful discussions. M.C. acknowledges support from the Netherlands Organisation for Scientific Research (NWO).

ORCID iDs

L. Boco  <https://orcid.org/0000-0003-3127-922X>
 A. Lapi  <https://orcid.org/0000-0002-4882-1735>
 D. Donevski  <https://orcid.org/0000-0001-5341-2162>

References

- Abbott, B. P., Abbott, R., Abbott, T. D., et al. 2016a, *PhRvL*, **116**, 241103
 Abbott, B. P., Abbott, R., Abbott, T. D., et al. 2016b, *PhRvL*, **116**, 061102
 Abbott, B. P., Abbott, R., Abbott, T. D., et al. 2016c, *PhRvX*, **6**, 041015
 Abbott, B. P., Abbott, R., Abbott, T. D., et al. 2017a, *ApJL*, **851**, L35
 Abbott, B. P., Abbott, R., Abbott, T. D., et al. 2017b, *ApJL*, **848**, L12
 Abbott, B. P., Abbott, R., Abbott, T. D., et al. 2017c, *PhRvL*, **119**, 161101
 Abbott, B. P., Abbott, R., Abbott, T. D., et al. 2017d, *PhRvL*, **119**, 141101
 Abbott, B. P., Abbott, R., Abbott, T. D., et al. 2017e, *PhRvL*, **118**, 221101
 Abbott, B. P., Abbott, R., Abbott, T. D., et al. 2019, *PhRvX*, **9**, 031040
 Abbott, B. P., Abbott, R., Abbott, T. D., et al. 2020a, arXiv:2010.14527
 Abbott, B. P., Abbott, R., Abbott, T. D., et al. 2020b, arXiv:2010.14533
 Alavi, A., Siana, B., Richard, J., et al. 2016, *ApJ*, **832**, 56
 Artale, M. C., Mapelli, M., Giacobbo, N., et al. 2019, *MNRAS*, **487**, 1675
 Asano, R. S., Takeuchi, T. T., Hirashita, H., & Inoue, A. K. 2013, *EP&S*, **65**, 213

- Barrett, J. W., Gaebel, S. M., Neijssel, C. J., et al. 2018, *MNRAS*, **477**, 4685
- Belczynski, K., Bulik, T., Fryer, C. L., et al. 2010a, *ApJ*, **714**, 1217
- Belczynski, K., Dominik, M., Bulik, T., et al. 2010b, *ApJL*, **715**, L138
- Belczynski, K., Holz, D. E., Bulik, T., & O’Shaughnessy, R. 2016, *Natur*, **534**, 512
- Bhatawdekar, R., Conselice, C., Margalef-Bentabol, B., & Duncan, K. 2019, *MNRAS*, **486**, 3805
- Bisigello, L., Caputi, K. I., Grogan, N., & Koekemoer, A. 2018, *A&A*, **609**, A82
- Boco, L., Lapi, A., & Danese, L. 2020, *ApJ*, **891**, 94
- Boco, L., Lapi, A., Goswami, S., et al. 2019, *ApJ*, **881**, 157
- Boogaard, L. A., Decarli, R., González-López, J., et al. 2019, *ApJ*, **882**, 140
- Bouquien, M., Burgarella, D., Roehly, Y., et al. 2019, *A&A*, **622**, A103
- Bouwens, R. J., Aravena, M., De Carli, R., et al. 2016, *ApJ*, **833**, 72
- Bouwens, R. J., Illingworth, G. D., Oesch, P. A., et al. 2015, *ApJ*, **803**, 34
- Bouwens, R. J., Oesch, P. A., Illingworth, G. D., Ellis, R. S., & Stefanon, M. 2017, *ApJ*, **843**, 129
- Bthermin, M., Daddi, E., Magdis, G., et al. 2012, *ApJL*, **757**, L23
- Bthermin, M., Daddi, E., Magdis, G., et al. 2015, *A&A*, **573**, A113
- Caffau, E., Ludwig, H. G., Steffen, M., Freytag, B., & Bonifacio, P. 2011, *SoPh*, **268**, 255
- Calore, F., Cuoco, A., Regimbau, T., Sachdev, S., & Serpico, P. D. 2020, *PhRvR*, **2**, 023314
- Calzetti, D., Armus, L., Bohlin, R. C., et al. 2000, *ApJ*, **533**, 682
- Cao, L., Lu, Y., & Zhao, Y. 2018, *MNRAS*, **474**, 4997
- Caputi, K. I., Deshmukh, S., Ashby, M. L. N., et al. 2017, *ApJ*, **849**, 45
- Casey, M. C., Zavala, J. A., Spilker, J., et al. 2018, *ApJ*, **862**, 67
- Cassarà, L. P., Maccagni, D., Garilli, B., et al. 2016, *A&A*, **593**, A9
- Chabrier, G. 2003, *ApJL*, **586**, L133
- Chabrier, G. 2005, in *The Initial Mass Function 50 Years Later*, ed. E. Corbelli & F. Palle (Dordrecht: Springer), 41
- Chiappini, C., Matteucci, F., & Gratton, R. 1997, *ApJ*, **477**, 765
- Chruslinska, M., Belczynski, K., Klencki, J., & Benacquista, M. 2018, *MNRAS*, **474**, 2937
- Chruslinska, M., & Nelemans, G. 2019, *MNRAS*, **488**, 5300
- Chruslinska, M., Nelemans, G., & Belczynski, K., 2019, *MNRAS*, **482**, 5012
- Citro, A., Pozzetti, L., Moresco, M., & Cimatti, A. 2016, *A&A*, **592**, A19
- Cooray, A., Calanog, J., Wardlow, J. L., et al. 2014, *ApJ*, **790**, 40
- Coppin, K. E. K., Geach, J. E., Almaini, O., et al. 2015, *MNRAS*, **446**, 1293
- Courteau, S., Cappellari, M., de Jong, R. S., et al. 2014, *RvMP*, **86**, 47
- Cremellini, P., & Vernizzi, F. 2017, *PhRvL*, **25**, 251302
- Cucciati, O., Tresse, L., Ilbert, O., et al. 2012, *A&A*, **539**, A31
- Curti, M., Mannucci, F., Cresci, G., & Maiolino, R. 2020, *MNRAS*, **491**, 944
- da Cunha, E., Charlot, S., & Elbaz, D. 2008, *MNRAS*, **388**, 1595
- da Cunha, E., Walter, F., Smail, I. R., et al. 2015, *ApJ*, **806**, 110
- Daddi, E., Alexander, D. M., Dickinson, M., et al. 2007, *ApJ*, **670**, 173
- Davé, R., Angls-Alcaraz, D., Narayanan, D., et al. 2019, *MNRAS*, **486**, 2827
- Davé, R., Rafieferantsoa, M. H., Thompson, R. J., & Hopkins, P. F. 2017, *MNRAS*, **467**, 115
- Davidzon, I., Ilbert, O., Laigle, C., et al. 2017, *A&A*, **605**, A70
- de Mink, S. E., & Belczynski, K. 2015, *ApJ*, **814**, 58
- de Mink, S. E., Langer, N., Izzard, R. G., Sana, H., & de Koter, A. 2013, *ApJ*, **764**, 166
- Dominik, M., Belczynski, K., Fryer, C., et al. 2012, *ApJ*, **759**, 52
- Dominik, M., Berti, E., O’Shaughnessy, R., et al. 2015, *ApJ*, **806**, 263
- Donevski, D., Lapi, A., Malek, K., et al. 2020, *A&A*, **644**, A144
- Dunlop, J. S., McLure, R. J., Biggs, A. D., et al. 2017, *MNRAS*, **466**, 861
- Dvorkin, I., Uzan, J.-P., Vangioni, E., & Silk, J. 2018, *MNRAS*, **479**, 121
- Efstathiou, A., Rowan-Robinson, M., & Siebenmorgen, R. 2000, *MNRAS*, **313**, 734
- Elbert, O. D., Bullock, J. S., & Kaplinghat, M. 2018, *MNRAS*, **473**, 1186
- Eldridge, J. J., & Stanway, E. R. 2016, *MNRAS*, **462**, 3302
- Eldridge, J. J., Stanway, E. R., Xiao, L., et al. 2017, *PASA*, **34**, e058
- Finkelstein, S. L., Ryan, R. E., Jr., Papovich, C., et al. 2015, *ApJ*, **810**, 71
- Fishbach, M., Gray, R., Magana Hernandez, I., et al. 2019, *ApJL*, **871**, L13
- Fudamoto, Y., Oesch, P. A., Schinnerer, E., et al. 2017, *MNRAS*, **472**, 483
- Gallazzi, A., Bell, E. F., Zibetti, S., Brinchmann, J., & Kelson, D. D. 2014, *ApJ*, **788**, 72
- Gallazzi, A., Charlot, S., Brinchmann, J., & White, S. D. M. 2006, *MNRAS*, **370**, 1106
- Genzel, R., Tacconi, L. J., Lutz, D., et al. 2015, *ApJ*, **800**, 20
- Giacobbo, N., & Mapelli, M. 2018, *MNRAS*, **480**, 2011
- Giacobbo, N., Mapelli, M., & Spera, M. 2018, *MNRAS*, **474**, 2959
- Ginolfi, M., Jones, G. C., Bethermin, M., et al. 2020, *A&A*, **633**, A90
- Grisoni, V., Spitoni, E., Matteucci, F., et al. 2017, *MNRAS*, **472**, 3637
- Gruppioni, C., Bethermin, M., Loiacono, F., et al. 2020, *A&A*, **643**, A8
- Gruppioni, C., Calura, F., Pozzi, F., et al. 2015, *MNRAS*, **451**, 3419
- Gruppioni, C., & Pozzi, F. 2019, *MNRAS*, **483**, 1993
- Gruppioni, C., Pozzi, F., Rodighiero, G., et al. 2013, *MNRAS*, **432**, 23
- Hunt, L., Dayal, P., Magrini, L., & Ferrara, A. 2016, *MNRAS*, **463**, 2002
- Hurley, J. R., Pols, O. R., & Tout, C. A. 2000, *MNRAS*, **315**, 543
- Ilbert, O., Arnouts, S., Le Floc’h, E., et al. 2015, *A&A*, **579**, A2
- Ilbert, O., McCracken, H. J., Le Fèvre, O., et al. 2013, *A&A*, **556**, A55
- Johansson, J., Thomas, D., & Maraston, C. 2012, *MNRAS*, **421**, 1908
- Jones, T., Sanders, R., Roberts-Borsani, G., et al. 2020, *ApJ*, **903**, 150
- Juarez, Y., Maiolino, R., Mujica, R., et al. 2009, *A&A*, **494**, L25
- Kennicutt, R. C. 1998, *ApJ*, **498**, 541
- Kennicutt, R. C., & Evans, N. J. 2012, *ARA&A*, **50**, 531
- Kewley, L. J., & Ellison, S. L. 2008, *ApJ*, **681**, 1183
- Kistler, M. D., Yüksel, H., & Beacom, J. F. 2009, *ApJL*, **705**, L104
- Kistler, M. D., Yüksel, H., & Hopkins, A. M. 2013, arXiv:1305.1630
- Klencki, J., Moe, M., Gladysz, W., et al. 2018, *A&A*, **619**, A77
- Lamberts, A., Garrison-Kimmel, S., Clausen, D. R., & Hopkins, P. F. 2016, *MNRAS*, **463**, L31
- Lamberts, A., Garrison-Kimmel, S., Hopkins, P. F., et al. 2018, *MNRAS*, **480**, 2704
- Lapi, A., Gonzalez-Nuevo, J., Fan, L., et al. 2011, *ApJ*, **742**, 24
- Lapi, A., Mancuso, C., Bressan, A., & Danese, L. 2017, *ApJ*, **847**, 13
- Lapi, A., Pantoni, L., Boco, L., & Danese, L. 2020, *ApJ*, **897**, 81
- Li, J., Wang, R., Cox, P., et al. 2020, *ApJ*, **900**, 131
- Li, S. S., Mao, S., Zhao, Y., & Lu, Y. 2018, *MNRAS*, **476**, 2220
- Liao, K., Fan, X.-L., Ding, X., Biesiada, M., & Zhu, Z.-H. 2017, *NatCo*, **8**, 1148
- Liu, D., Daddi, E., Dickinson, M., et al. 2018, *ApJ*, **853**, 172
- Liu, D., Schinnerer, E., Groves, B., et al. 2019, *ApJ*, **887**, 235
- Madau, P., & Dickinson, M. 2014, *ARA&A*, **52**, 415
- Maeder, A. 1992, *A&A*, **264**, 105
- Magnelli, B., Lutz, D., Berta, S., et al. 2012, *A&A*, **548**, A22
- Magnelli, B., Popesso, P., Berta, S., et al. 2013, *A&A*, **553**, A132
- Maiolino, R., & Mannucci, F. 2019, *A&ARV*, **27**, 3
- Maiolino, R., Nagao, T., Grazian, A., et al. 2008, *A&A*, **488**, 463
- Mancuso, C., Lapi, A., Shi, J., et al. 2016a, *ApJ*, **823**, 128
- Mancuso, C., Lapi, A., Shi, J., et al. 2016b, *ApJ*, **833**, 152
- Mannucci, F., Cresci, G., Maiolino, R., et al. 2009, *MNRAS*, **398**, 1915
- Mannucci, F., Cresci, G., Maiolino, R., Marconi, A., & Gnerucci, A. 2010, *MNRAS*, **408**, 2115
- Mannucci, F., Salvaterra, R., & Campisi, M. A. 2011, *MNRAS*, **414**, 1263
- Mapelli, M., & Giacobbo, N. 2018, *MNRAS*, **479**, 4391
- Mapelli, M., Giacobbo, N., Ripamonti, E., & Spera, M. 2017, *MNRAS*, **472**, 2422
- Marrone, D. P., Spilker, J. S., Hayward, C. C., et al. 2018, *Natur*, **553**, 51
- Meurer, G. R., Heckman, T. M., & Calzetti, D. 1999, *ApJ*, **521**, 64
- Mo, H., van den Bosch, F., & White, S. D. M. 2010, *Galaxy Formation and Evolution* (Cambridge: Cambridge Univ. Press)
- Morishita, T., Abramson, L. E., Treu, T., et al. 2019, *ApJ*, **877**, 141
- Moustakas, J., Coil, A. L., Aird, J., et al. 2013, *ApJ*, **767**, 50
- Muzzin, A., Marchesini, D., & Stefanon, M. 2013, *ApJ*, **777**, 18
- Neijssel, C. J., Vigna-Gomez, A., Stevenson, S., et al. 2019, *MNRAS*, **490**, 3740
- Nissanke, S., Holz, D. E., Dalal, N., et al. 2013, arXiv:1307.2638
- Novak, M., Bañados, E., Decarli, R., et al. 2019, *ApJ*, **881**, 63
- Novak, M., Smolcic, V., Delhaize, J., et al. 2017, *A&A*, **602**, 5
- O’Shaughnessy, R., Bellovary, J. M., Brooks, A., et al. 2017, *MNRAS*, **464**, 2831
- O’Shaughnessy, R., Kalogera, V., & Belczynski, K. 2010, *ApJ*, **716**, 615
- Oesch, P. A., Bouwens, R. J., Carollo, C. M., et al. 2010, *ApJL*, **725**, L150
- Oguri, M. 2016, *PhRvD*, **93**, 083511
- Onodera, M., Carollo, C. M., Lilly, S., et al. 2016, *ApJ*, **822**, 42
- Onoue, M., Bañados, E., Mazzucchelli, C., et al. 2020, *ApJ*, **898**, 105
- Pantoni, L., Lapi, A., Massardi, M., Goswami, S., & Danese, L. 2019, *ApJ*, **880**, 129
- Papovich, C., Finkelstein, S. L., Ferguson, H. C., Lotz, J. M., & Giavalisco, M. 2011, *MNRAS*, **412**, 1123
- Pezzulli, G., & Fraternali, F. 2016, *MNRAS*, **455**, 2308
- Planck Collaboration 2019, *A&A*, **641**, A6
- Popping, G., Somerville, R. S., & Galametz, M. 2017, *MNRAS*, **471**, 3152
- Portegies Zwart, S. F., & Yungelson, L. R. 1998, *A&A*, **332**, 173
- Raccanelli, A., Kovetz, E. D., Bird, S., Cholis, I., & Muñoz, J. B. 2016, *PhRvD*, **94**, 023516
- Radice, David, Perego, Albino, Zappa, Francesco, & Bernuzzi, Sebastiano 2018, *ApJL*, **852**, L29

- Reddy, N. A., Kriek, M., Shapley, A. E., et al. 2015, *ApJ*, 806, 259
- Riechers, D. A., Leung, T. K. D., Ivison, R. J., et al. 2017, *ApJ*, 850, 1
- Rodighiero, G., Brusa, M., Daddi, E., et al. 2015, *ApJL*, 800, L10
- Rodighiero, G., Daddi, E., Baronchelli, I., et al. 2011, *ApJL*, 739, L40
- Romano, D., Silva, L., Matteucci, F., & Danese, L. 2002, *MNRAS*, 334, 444
- Rowan-Robinson, M., Oliver, S., Wang, L., et al. 2016, *MNRAS*, 461, 1100
- Sander, A. A. C., Vink, J. S., & Hamann, W.-R. 2020, *MNRAS*, 491, 4406
- Sanders, R. L., Shapley, A. E., Jones, T., et al. 2020a, arXiv:2009.07292
- Sanders, R. L., Shapley, A. E., Reddy, N. A., et al. 2020b, *MNRAS*, 491, 1427
- Santoliquido, F., Mapelli, M., Giacobbo, N., Bouffanais, Y., & Artale, M. C. 2020, arXiv:2009.03911
- Saracco, P., Marchesini, D., La Barbera, F., et al. 2020, *ApJ*, 905, 40
- Sargent, M. T., Bethermin, M., Daddi, E., & Elbaz, D. 2012, *ApJL*, 747, L31
- Scelfo, G., Bellomo, N., Raccanelli, A., Matarrese, S., & Verde, L. 2018, *JCAP*, 2018, 039
- Scelfo, G., Boco, L., Lapi, A., & Viel, M. 2020, *JCAP*, 2020, 045
- Schiminovich, D., Ilbert, O., Arnouts, S., et al. 2005, *ApJL*, 619, L47
- Schreiber, C., Pannella, M., Elbaz, D., et al. 2015, *A&A*, 575, 74
- Shapley, A. E., Cullen, F., Dunlop, J. S., et al. 2020, *ApJL*, 903, L16
- Silva, L., Granato, G. L., Bressan, A., & Danese, L. 1998, *ApJ*, 509, 103
- Smail, I., Dudzevičiūtė, U., Stach, S. M., et al. 2012, arXiv:2010.02250
- Smit, R., Bouwens, R. J., Franx, M., et al. 2012, *ApJ*, 756, 14
- Speagle, J. S., Steinhardt, C. L., Capak, P. L., & Silverman, J. 2014, *ApJS*, 214, 15
- Spera, M., & Mapelli, M. 2017, *MNRAS*, 470, 4739
- Spera, M., Mapelli, M., Giacobbo, N., et al. 2019, *MNRAS*, 485, 889
- Stacey, H. R., McKean, J. P., Robertson, N. C., et al. 2018, *MNRAS*, 476, 5075
- Steinhardt, C. L., Speagle, J. S., & Capak, P. 2014, *ApJL*, 791, L25
- Strait, V., Bradac, M., Coe, D., et al. 2020, arXiv:2009.00020
- Sundqvist, J. O., Björklund, R., Puls, J., & Najarro, F. 2019, *A&A*, 632, A126
- Tacconi, L. J., Genzel, R., & Sternberg, A. 2020, *ARA&A*, 58, 157
- Tan, Q., Daddi, E., Magdis, G., et al. 2014, *A&A*, 569, A98
- Taylor, S. R., & Gair, J. R. 2012, *PhRvD*, 86, 023502
- Thomas, D., Maraston, C., Bender, R., & Mendes de Oliveira, C. 2005, *ApJ*, 621, 673
- Thomas, D., Maraston, C., Schawinski, K., Sarzi, M., & Silk, J. 2010, *MNRAS*, 404, 1775
- Tomczak, A. R., Quadri, R. F., Tran, K. H., et al. 2014, *ApJ*, 783, 85
- Torrey, P., Vogelsberger, M., Hernquist, L., et al. 2018, *MNRAS*, 477, L16
- van der Burg, R. F. J., Hildebrandt, H., & Erben, T. 2010, *A&A*, 523, A74
- Venemans, B. P., Decarli, R., Walter, F., et al. 2018, *ApJ*, 866, 159
- Venemans, B. P., Walter, F., Decarli, R., et al. 2017, *ApJL*, 851, L8
- Vijayan, A. P., Clay, S. J., Thomas, P. A., et al. 2019, *MNRAS*, 489, 4072
- Vink, J. S., & de Koter, A. 2005, *A&A*, 442, 587
- Vink, J. S., de Koter, A., & Lamers, H. J. G. L. M. 2001, *A&A*, 369, 574
- Wang, T., Schreiber, C., Elbaz, D., et al. 2019, *Natur*, 572, 211
- Whitaker, K. E., Franx, M., Leja, J., et al. 2014, *ApJ*, 795, 104
- Wyder, T. K., Treyer, M. A., Milliard, B., et al. 2005, *ApJL*, 619, L15
- Yang, T., Hu, B., Cai, R., & Wang, B. 2019, *ApJ*, 880, 50
- Zahid, H. J., Kashino, D., Silverman, J. D., et al. 2014, *ApJ*, 792, 75
- Zavala, J. A., Montana, A., Hughes, D. H., et al. 2018, *NatAs*, 2, 56